Spring 2015

Characterization of wake effects and loading status of wind turbine arrays under different inflow conditions

Xiangyu Gao
Purdue University

Graduate School Form 30
Updated 1/15/2015

PURDUE UNIVERSITY
GRADUATE SCHOOL
Thesis/Dissertation Acceptance

This is to certify that the thesis/dissertation prepared

By Xiangyu Gao

Entitled

Characterization of Wake Effects and Loading Status of Wind Turbine Arrays Under Different Inflow Conditions

For the degree of Master of Science in Engineering

Is approved by the final examining committee:

Jun Chen Chair	J. Stuart Bolton
Tom Shih	

To the best of my knowledge and as understood by the student in the Thesis/Dissertation Agreement, Publication Delay, and Certification Disclaimer (Graduate School Form 32), this thesis/dissertation adheres to the provisions of Purdue University's "Policy of Integrity in Research" and the use of copyright material.

Approved by Major Professor(s): Jun Chen

Approved by: Ganesh Subbarayan 4/23/2015

Head of the Departmental Graduate Program Date

CHARACTERIZATION OF WAKE EFFECTS AND LOADING STATUS OF WIND TURBINE ARRAYS UNDER DIFFERENT INFLOW CONDITIONS

A Thesis

Submitted to the Faculty

of

Purdue University

by

Xiangyu Gao

In Partial Fulfillment of the

Requirements for the Degree

of

Master of Science in Engineering

May 2015

Purdue University

West Lafayette, Indiana

To my family for their selfless support,

to my major professor for leading me into the fantastic world of turbulence and fluid dynamics,

to my friends for their accompany and the god like Medusa

ACKNOWLEDGMENTS

First and foremost, I would like to thank my advisor, Dr. Jun Chen, for giving me helpful and patient instructions and fostering my intellectual growth throughout my time at Purdue University. I appreciate the opportunities you gave me to write research articles and present my research results in conference, which are precious experiences for my future research. I also want to give my thanks to Nina, Ranchi, Yongkai and Zach, for the helpful and efficient discussions. I cannot finish my master thesis without your help.

I would also like to thank Dr. Tom Shih and Dr. J. Stuart Bolton for serving on my advisory committee and supporting my PhD application. I really want to thank Prof. Chen, Prof. Shih and Prof. Bolton for your recommendations, because every professor who interviewed me during my PhD application told me that I had strong recommendations. Thank you also to Yuqiang, Tianqi, Yikuan, Songlin and Ning for your friendship, assistance and support.

Finally, the biggest thank goes to my parents, Yi and Yuemei. Your selfless supports are the motivation for all my hard work and insistence. You have been with me and encouraging me all the time. Your smiles and happiness mean the world to me.

TABLE OF CONTENTS

LIST OF TABLES

LIST OF FIGURES

SYMBOLS

$\tilde{\cdot}$	filtering operation
$< \cdot >$	averaging operation
$\star$	outer product
α	angle of attack
β	pitch angle
γ	twist angle
Δ	grid spacing
Δ_b	length of segments on actuator lines
η_ε	Gaussian Weight Function
η	spatial distribution of vortices
ι	size of vortices
κ	von Karman constant
μ_t	eddy viscosity
ν	kinematic viscosity
ρ	density of fluid
σ	solidity of rotor
ς	size of vortices
Ω	angular velocity of blades

ϕ	angle between U_{rel} and rotor plane
$\phi(s)$	three point discrete delta function
τ_{ij}	SGS stress
ω	vorticity vector
Γ	circulation
ξ	distance between cell center and actuator point
ε	constant to adjust the strength of Gaussian Weight Function
a	axial velocity induction factor
a'	tangential velocity induction factor
C_d	drag coefficient
C_l	lift coefficient
C_N	axial force coefficient
C_T	tangential force coefficient
C_s	Smagorinsky constant
c	chord length
D	diameter of rotor
dD	drag force on one blade element
dL	lift force on one blade element
F	Prandtl's correction factor
F_1	F_1 correction factor
$\vec{F_{2D}}$	total force on one blade element
$\vec{F_\varepsilon}$	bodyforce distributed in each cell

F_n	axial force on one blade element
F_t	tangential force on one blade element
f_i	body force
$f(\mathbf{x}, t)$	one specific quantity in flow field
$\vec{g}$	unit vector in the direction of the gradient of mean velocity field
k	TKE
L_x	domain length
L_y	domain width
L_z	domain height
M	number of vortices
N	number of blades
N_x	grid number in x direction
N_y	grid number in y direction
N_z	grid number in z direction
$\vec{n}$	unit vector in axial direction
p	pressure
$\mathcal{P}$	production term
R	radius of blade
$\mathcal{R}_{ij}$	Reynolds stress
Re	Reynolds number
r	radius of blade element
S_{ij}	strain rate

T_i	turbulence transport term
T_{ij}	label for turbine in wind farm
$\vec{t}$	unit vector in tangential direction
t	time
U_∞	free stream velocity
U_θ	tangential velocity extracted from flow field with LEI and LVS
U_{rel}	relative velocity between incoming wind and blade element
$\vec{U}(\vec{X})$	velocity vector in Eulerian coordinate
U_x	axial velocity extracted from flow field with LEI and LVS
$\vec{U}(\vec{x})$	velocity vector in Lagrangian coordinate
u'	velocity fluctuation in x direction
$\vec{u}(\vec{x})$	vector of velocity fluctuation
u_i	velocity field
u^*	friction velocity
V	volume of a cell
v'	velocity fluctuation in y direction
w'	velocity fluctuation in z direction
$\vec{X}$	coordinate in Eulerian point of view
$\vec{x}$	coordinate in Lagrangian point of view
x	streamwise direction
y	horizontal direction
z	vertical direction

z_{hub}	z coordinate of turbine hub
z_{ground}	z coordinate of ground
z_0	roughness length

ABBREVIATIONS

ABL	Atmospheric Boundary Layer
ADM	Actuator Disk Model
ALM	Actuator Line Model
ASM	Actuator Surface Model
BEM	Blade Element Momentum
CFD	Computational Fluid Dynamics
DILU	Diagonal Incomplete LU (Lower/Upper) Decomposition
GAMG	Geometric-Algebraic Multi-Grid
LEI	Lagrangian-Eulerian Interpolation
LVS	Local Velocity Sampling
NREL	National Renewable Energy Laboratory
NS	Navier-Stokes
OpenFOAM	Open Field Operations and Manipulations
PBiCG	Pre-conditioned BiConjugate-Gradient
PISO	Pressure-Implicit Splitting Operation
PIV	Particle Image Velocimetry
SGS	Sub-Grid Scale
TKE	turbulent kinetic energy

ABSTRACT

Gao, Xiangyu MSE, Purdue University, May 2015. Characterization of Wake Effects and Loading Status of Wind Turbine Arrays Under Different Inflow Conditions. Major Professor: Jun Chen, School of Mechanical Engineering.

The objective of the present work is to improve the accuracy of Actuator Line Modeling (ALM) in predicting the unsteady aerodynamic loadings on turbine blades and turbine wake by assessing different methods used to determine the relative velocity between the rotating blades and wind. ALM is incorporated into a Large Eddy Simulation (LES) solver in OpenFOAM (Open Field Operations and Manipulations). The aerodynamic loadings are validated by experiment results from National Renewable Energy Laboratory (NREL). Turbine wakes are validated by predictions of large eddy simulation using exact 3D blade geometries from a two-blade NREL Phase VI turbine. Three different relative velocity calculation methods are presented: iterative process in Blade Element Momentum (BEM) theory, local velocity sampling, and Lagrange-Euler Interpolation (LEI). Loadings and wakes obtained from these three methods are compared. It is discovered that LEI functions better than the conventional BEM with iterative process in both loading and wake prediction. Then LES-ALM with LEI is performed on a small wind farm deploying five NREL Phase VI turbines in full wake setting. The power outputs and force coefficients of downstream turbines are evaluated. The LES-ALM with LEI is also performed on a small wind

farm deploying 25 (5×5) NREL Phase VI turbines with different inflow angles (from full wake setting to partial wake setting). The power outputs and force coefficients of each turbine are evaluated under different inflow angles (the angle the rotor has to turn to make the rotor plane face the incoming wind) (0^o, 5^o, 15^o, 30^o and 45^o). The power coefficient distributions and thrust coefficient distributions of the wind farm under each inflow angle are compared. The range of inflow angle which is best for power generation is also discussed. The results demonstrate that the LES-ALM with LEI has the potential to optimize wind farm arrangement and pitch angle of individual turbines.

1. INTRODUCTION

1.1 Overview

During the last two decades, wind energy has gained increased research attention. Popular as it is, designing large-scale wind farms faces two major challenges: reduced power output of downstream turbines due to the velocity deficit, and escalated dynamic loadings due to higher turbulence intensity [1]. Wind turbine clustered in wind farm work under a unsteady flow field, which is affected by the wake of upstream turbines. As a result, these downstream turbines experience different working condition from stand alone turbines, which will bring reduced power generation and increased fatigue loads. A 10% power output deficit was reported for three turbines separated by $7D$ (D is the turbine diameter) in full wake setting [2]. The aerodynamic loadings on downstream turbines were reported to increase by 45% for a turbine spacing of $5D$ [3]. It is thus of significance to accurately analyze the wake effect and dynamic loading applied on each individual wind turbines within turbine arrays.

1.2 Experimental Study

Generally, there are two mainstream approaches to study wake and loading characteristics of wind turbines: experimental measurement and numerical simulation.

Full-size field measurements and scaled model experiments wind tunnel are conducted all over the world to gain insights about turbine wakes [4–7]. Experimental studies give people great details and insights into the flow field around a wind turbine, which can used to validate simulation results. Masts measurements are popularly used in industry for on-site measurements in wind farms. However, they are insufficient for detailed measurements because of the limited number of sampling locations. Techniques like LiDAR and Sodar are applied in wind turbine measurements, but their spatial-temporal resolution is usually coarse [8–10]. It is challenging to apply them in industry projects, so is very large scale Particle Image Velocimetry (PIV) [11]. Meanwhile, scaled model experiments in wind tunnel lead to detailed measurements of flow field, but are limited by: (a) size limitation of experimental models, (b) relatively low Reynolds numbers generated in wind tunnel experiments, (c) idealized experiment environments, which may be very different from actual operational conditions of wind turbines, and (d) inadequate experiment techniques to resolve the temporal-spatial features of the unsteady three-dimensional flow field.

1.3 Computational Fluid Dynamics for Wind Turbine Wake Aerodynamics

Computational Fluid Dynamics (CFD) is another powerful tool to analyze turbine wake and loading [12–15]. According to the way turbulence is modeled, CFD-based simulations can be divided into Reynolds-Averaged Navier-Stokes (RANS), Large Eddy Simulation (LES) and Direct Numerical Simulation (DNS). In RANS simulations, one specific flow quantity $f(\mathbf{x}, t)$ is decomposed into a time-averaged part

$< f(\mathbf{x},t) >$ and a fluctuation part $f'(\mathbf{x},t)$, which is the so-called Reynolds decomposition: $f(\mathbf{x},t) =< f(\mathbf{x},t) > +f'(\mathbf{x},t)$, where $< \cdot >$ denotes the time averaging operation. With appropriate turbulence model, the time averaged variables can be solved from RANS equations. RANS is widely used in wind turbine wake simulation because of its low computational cost [16, 17]. In LES, one specific flow quantity $f(\mathbf{x},t)$ is decomposed into a resolved part $\tilde{f}(\mathbf{x},t)$ and a sub-grid scale (SGS) part $f^{SGS}(\mathbf{x},t)$: $f(\mathbf{x},t) = \tilde{f}(\mathbf{x},t) + f^{SGS}(\mathbf{x},t)$, where $\tilde{\cdot}$ denotes the filtering operation. Even though is more expensive than RANS, but it can provide more accurate flow fields, so it is also widely used [13, 18, 19]. DNS is the most accurate, and at the same time, most expensive. It resolves all the scales in the fluid flow. Because of the broad range of scales included in CFD-based wind turbine simulations, DNS is not affordable based on current computational power. According to the discussion above, LES should be the best one to study wake effects in current stage.

CFD simulations of flow field around wind turbines can also be sorted into five categories, ordered by increasing complexity and computational cost: (1) Blade Element Momentum (BEM) theory, (2) Actuator Disc Modeling (ADM), (3) Actuator Line Modeling (ALM), (4) Actuator Surface Modeling (ASM), and (5) full Navier-Stokes (NS) simulation with all geometric details considered. Among them, the last one, geometry-resolved NS approach, yields the most accurate results for studying flow around individual wind turbine (e.g., Refs. [17, 20, 21]). However, due to its high computational cost, at the present stage, this method cannot be extended to simulate wind farm with clusters of wind turbines. On the other hand, a BEM routine [22]

has been successfully developed as a design tool: (a) a rotor blade is divided into multiple sections along spanwise direction; (b) one-dimensional momentum balance is performed on each individual section using tabulated airfoil data, which are determined experimentally on that specific airfoil, to relate the aerodynamic forces (lift and drag) to the effective angle of attack; and (c) the aerodynamic loading and power on the entire turbine are then obtained by integrating contributions of aerodynamic forces from each section. BEM is a relatively reliable method to characterize the performance of wind turbine and has been widely applied. However, it represents a quasi-steady analysis, so cannot be applied to study time-dependent phenomena (e.g., velocity fluctuation introduced by turbulence, rotor-rotor interaction, rotor-tower interaction, etc.). It also lacks the ability to predict the wake flow behind wind turbines. As an extension of BEM method, Sørensen *et al.* [23] proposed ADM, in which body forces are firstly distributed on a permeable disk as a surrogate of the turbine rotor by employing BEM theory. Then the forces are further distributed into all the cells in the computational domain via a regularization function. The body forces can be applied into the three-dimensional Navier-Stokes equations to solve for the flow around turbines. Compared to the geometry-resolved NS simulations, ADM requests significantly reduced number of computation grids and computational costs. It has been validated and applied to a variety of problems (e.g., [24, 25]). Stevens *et al.* [15] also presented the potential application of ADM in wind farm projects, in which the simulation was performed on a wind farm composed of 78 turbines. In order to further increase the simulation accuracy and to predict the unsteady flow characteristics,

ALM was developed [16], by distributing the aerodynamic forces along each turbine blade to yield a more physical description of the existence turbines blade. More details about ALM can be found in [26–28]. In particular, ALM has been applied to investigate turbine-turbine interaction in a large-scale wind farm [29]. ASM was proposed by Shen *et al.* [30], to achieve an accuracy and computational cost between ALM and geometry-resolved NS approach. So far it has not been widely used as ALM and ADM [31]. The concepts of ADM, ALM and ASM are sketched in figure 1.1.

1.4 Accurate ALM Simulation

Pursuing improved accuracy of ALM represents the state-of-the-art in large scale wind farm simulation by selecting proper parameters. There are three parameters when ALM is applied: (1) grid spacing Δ, (2) length of segments on actuator line Δ_b, and (3) the radius of body force distribution function ε. Guidelines for proper selection of these parameters were explored. Martinez *et al.* [32] reported that wake profile predicted by ALM is sensitive to ε when $\Delta/\varepsilon \leq 2$, and Shives *et al.* [33] showed that when $\Delta/\varepsilon \geq 4$, ALM can give accurate predictions. Jha *et al.* [14] suggested $\Delta_b/\Delta \geq 1.5$. There are also three approaches to determine the radius of body force distribution function: (1) Gird-Based Radius [24, 25], $\varepsilon/\Delta = const$, (2) Chord-Based Radius [33], $\varepsilon/c = const$, (3) Elliptic Gaussian Radius [14].

In recent years, ALM has been incorporated into Large Eddy Simulation solver of Navier-Stokes equations (LES-ALM) to study the unsteady wake effect and aerodynamic loading in wind farms (e.g., [13, 18, 19]). LES-ALM represents a multi-fidelity

approach, which incorporates a low fidelity BEM into a high fidelity LES solver for Navier-Stokes equations. As a result, the accuracy of the low fidelity simulation will have a significant impact on the overall accuracy of the simulation results. In particular, successful application of BEM rely heavily on the estimated relative velocity (magnitude and direction) between the unsteady inflow and rotating blade element. This relative velocity is traditionally determined in an iteration process in BEM [12, 34]. However, there is one major drawback of this quasi-steady approach: it does not utilize the local flow field predicted by NS solver at all, and thus results in breaking down or deteriorated accuracy in unsteady flow, which represent the realistic operational condition of all wind turbines. To get rid of this drawback, a new method was proposed to tune BEM with the velocity field generated by the NS solver for computing the body forces, and finally solve the NS equations with these body forces applied. In addition, there are two ways to tune BEM. The first one, referred to Local Velocity Sampling (LVS) method in this paper, samples the relative velocity from the LES results at the center of the segment along the actuator line [14]. The second one, referred to as Lagrange-Euler Interpolation (LEI) method, interpolates the velocity along the actuator line from the background field using discrete delta function, which is often used in immersed boundary method [13]. With all these methods proposed to determine the relative velocity, there lacks direct comparison of their performance in LES-ALM. In this thesis, we provide such a systematic evaluation. In particular, LES-ALM is incorporated into a OpenFOAM solver to study the flow around a NREL Phase VI turbine turbine. First, the aerodynamic loadings predicted by ALMs with

iterative process, LVS, and LEI, are compared to experimental results. Predicted turbine wakes are compared to predictions from a Large Eddy Simulation using exact 3D blade geometries of the same turbine under identical conditions. It is identified that LEI is better than iterative process and LVS. Then LEI is used to simulate a flow over a small wind farm clustered by five NREL Phase VI turbines in full wake setting under turbulent inflow condition, to characterize the wake and loadings. The flow fields are also simulated for a wind farm deploying 25 (5×5) NREL Phase VI turbines under different arrangements (from full wake setting to partial wake setting) to test which arrangement is the best for power output.

1.5 Turbulent Inlet Boundary Condition

All the utility-scale wind farms operate in Atmospheric Boundary Layer (ABL), where strong turbulence is present. To enable wind turbine simulations with more realistic inflow conditions, turbulent inlet condition should be adopted. One of the most important characteristics of turbulence is random velocity fluctuation, but not all the velocity fluctuations are turbulent, the fluctuations must meet many requirements to be turbulent. In LES, turbulent inlet condition should meet the following criteria: (a) The fluctuation must be stochastic; and (b) It should be compatible with Navier-Stokes equations; (c) It must possess spatial and temporal correlations in turbulence; (d) It should be easy to implement, methods used to generate this turbulent inlet boundary condition in LES can be divided into two major categories: synthesized turbulence methods [35,36] and precursor simulation methods [37,38]. In

synthesized turbulence methods, the turbulent fluctuations are modeled in different mathematical ways, like Fourier techniques [35] and principle orthogonal decomposition [39]. Because these methods are purely mathematical, the fluctuations generated by these methods cannot represent totally realistic turbulence. In precursur simulation methods, the inlet velocity distribution is generated by running a separate, precursor simulation to get a library of turbulent data, which can be fed into the main wind farm simulation as inlet boundary. This is a more realistic way to generate turbulent inlet, but it is more expensive in computational cost and more difficult to implement. In this work, a vortex method, which was put forward by Sergent [40], and then implemented by Mathey *et al.* [41], is adopted. The vortex method is easier to implement than synthesized turbulence method and more efficient than the precursor simulation methods in terms of computational cost.

1.6 Motivation

As mentioned above, although LES-ALM has been applied to wind farm simulations for several years, there are few efforts on how to obtain more accurate relative velocity between incoming wind and rotating blade element. Even though there are different methods to get relative velocity, no systematic evaluation among these methods were done, so our motivation is to identify the most accurate method to obtain the relative velocity among current methods. Finally, it is found out that LEI is the best method. The second motivation of this work is to implement LES-ALM with LEI into OpenFOAM, an open source CFD software. There were several existing

works using OpenFOAM with LES-ALM, but none of them adopted LEI. With the proposed solver in OpenFOAM, one can study larger wind farm. In particular, the flow fields are simulated for a wind farm deploying 25 (5×5) NREL Phase VI turbines under different arrangements (from full wake setting to partial wake setting) to study the wake effects under different inflow conditions. The third motivation is to implement a turbulent inlet boundary condition in OpenFOAM to get more realistic working condition of wind farms.

1.7 Outline

This thesis is organized as follows: Chapter 2 describes the concept and mathematical details of ALM. It is also explained that why the relative velocity between the incoming wind and rotating blade element is important to the accurate ALM simulations. Then details about iterative process in BEM, LVS and LEI are presented. Mathematical descriptions of vortex method are also provided. In Chapter 3, we present the numerical setup (numerical schemes, numerical algorithms and linear algebra solvers adopted) and cases simulated in this work. In Chapter 4, presented is detailed analysis of the all the cases simulated. First, the results of flows over a stand-alone turbine are presented. Wakes and aerodynamics loadings obtained from iterative process in BEM, LVS and LEI are compared with those from LES with exact turbine geometry and experiment. It is identified that LEI performs best. Then LES-ALM with LEI is performed on a small wind farm clustered by five NREL Phase VI turbines in full wake setting under turbulent inflow condition, to characterize the

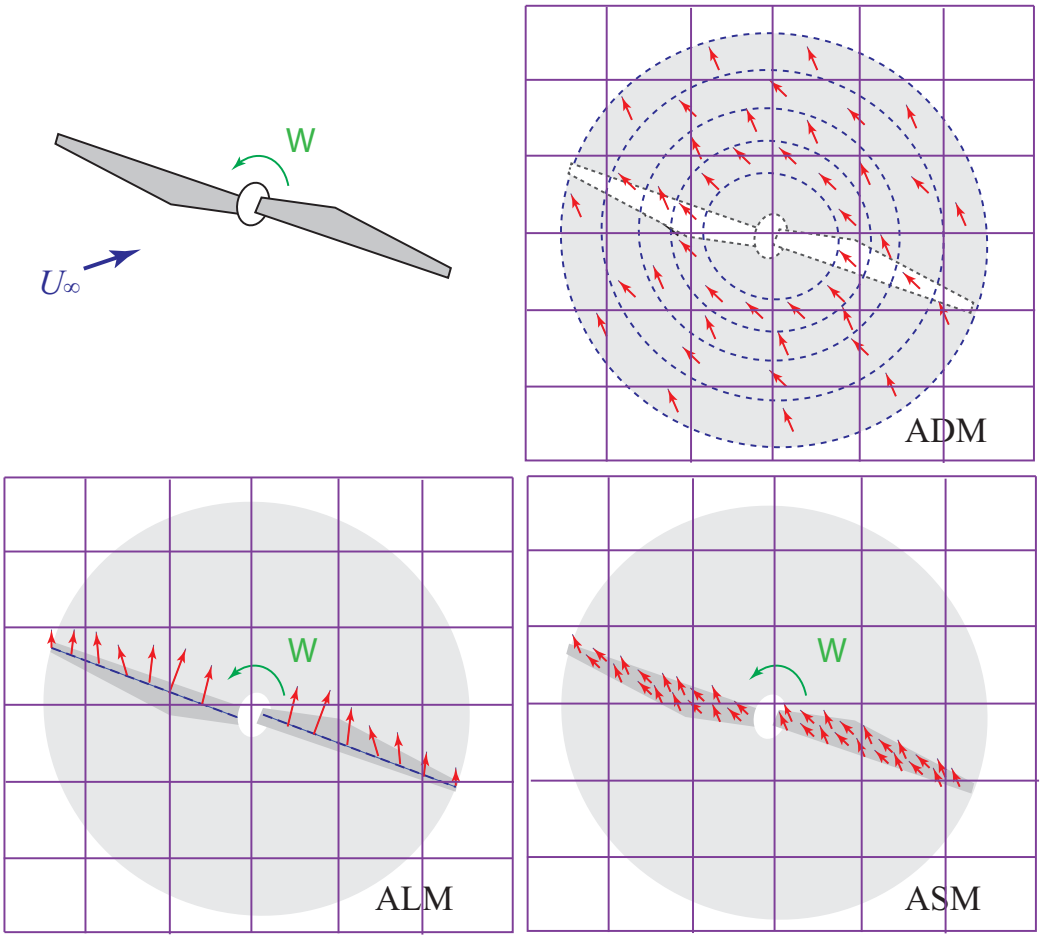

Figure 1.1. Principles of ADM, ALM and ASM. Vectors represent the distributed body forces as surrogate of rotating blades.

wake and loadings. Finally, this LES-ALM with LEI is adopted on a wind farm with $25(5 \times 5)$ wind turbines under different inflow angles, from full wake setting to partial wake setting. Wake effects, power coefficients, and thrust coefficients distributions are obtained for each inflow angle. The optimal range of inflow angle for power generation is then proposed. Chapter 5 draws the main conclusions and an outlook for future research.

2. METHOD

2.1 Governing Equation of LES and SGS Model

For incompressible flow, the Navier-Stokes equations are:

$$\frac{\partial u_i}{\partial x_i} = 0, \tag{2.1}$$

$$\frac{\partial u_i}{\partial t} + u_j \frac{\partial u_i}{\partial x_j} = -\frac{1}{\rho}\frac{\partial p}{\partial x_i} + \nu \frac{\partial^2 u_i}{\partial x_j \partial x_j} + f_i, \tag{2.2}$$

As introduced in 1, in LES, one specific flow quantity $f(\mathbf{x}, t)$ is decomposed into a resolved part $\tilde{f}(\mathbf{x}, t)$ and a sub-grid scale (SGS) part $f^{SGS}(\mathbf{x}, t)$: $f(\mathbf{x}, t) = \tilde{f}(\mathbf{x}, t) + f^{SGS}(\mathbf{x}, t)$, where $\tilde{\cdot}$ denotes the filtering operation. After applying the filtering operation to Navier-Stokes equation, one can get the filtered Navier-Stokes equations:

$$\frac{\partial \tilde{u}_i}{\partial x_i} = 0, \tag{2.3}$$

$$\frac{\partial \tilde{u}_i}{\partial t} + \tilde{u}_j \frac{\partial \tilde{u}_i}{\partial x_j} = -\frac{1}{\rho}\frac{\partial \tilde{p}}{\partial x_i} + \nu \frac{\partial^2 \tilde{u}_i}{\partial x_j \partial x_j} - \frac{1}{\rho}\frac{\partial \tau_{ij}}{\partial x_j} + f_i, \tag{2.4}$$

where $\tilde{u_i}$ and $\tilde{p}$ are the filtered velocity field and pressure field, respectively. f_i is the body force and τ_{ij} is the subgrid-scale (SGS) stress

$$\tau_{ij} = \widetilde{u_i u_j} - \tilde{u}_i \tilde{u}_j. \tag{2.5}$$

In order to close Equations (2.3) and (2.4), τ_{ij} must be modeled, e.g., popularly, by eddy-viscosity assumption:

$$\tau_{ij} - \frac{1}{2}\tau_{kk}\delta_{ij} = -2\mu_t \tilde{S}_{ij} = -\mu_t \left(\frac{\partial \tilde{u}_i}{\partial x_j} + \frac{\partial \tilde{u}_j}{\partial x_i} \right), \tag{2.6}$$

where μ_t is the eddy viscosity. μ_t can be further modeled by Smagorinsky model [42]

$$\mu_t = (C_s \Delta)^2 \tilde{S} \tag{2.7}$$

where C_s is the Smagorinsky constant, which is set to be 0.1678, and filter scale $\Delta = (\Delta x_1 \Delta x_2 \Delta x_3)^{1/3}$, in which Δx_i's represent the spatial resolutions in three orthogonal directions (i=1,2,3). $\tilde{S} = \sqrt{2\tilde{S}_{ij}\tilde{S}_{ij}}$ is the magnitude of the resolved strain rate where $\tilde{S}_{ij}$ is resolved the strain rate:

$$\tilde{S}_{ij} = \frac{1}{2} \left(\frac{\partial \tilde{u}_i}{\partial x_j} + \frac{\partial \tilde{u}_j}{\partial x_i} \right). \tag{2.8}$$

2.2 Actuator Line Modeling

The total force per unit radial length exerted on each spanwise element of the turbine blade can be decomposed into axial and tangential components:

$$\vec{F}_{2D} = \frac{dF_n}{dr}\vec{n} + \frac{dF_t}{dr}\vec{t}, \tag{2.9}$$

where $\vec{n}$ and $\vec{t}$ are the unit vectors in axial direction and tangential direction, respectively. dF_n/dr and dF_t/dr are components per unit length along the spanwise direction and they can be obtained by different methods, including BEM (from an iterative process), LVS or LEI, which will be discussed in detail in the following subsections.

In ALM, each blade is modeled as a rotating line on which the the body forces are distributed. To avoid singularities, a Gaussian weight function,

$$\eta_\varepsilon(\xi) = \frac{1}{\varepsilon^3 \pi^{3/2}} \exp[-(\xi/\varepsilon)^2], \tag{2.10}$$

is applied to distribute the forces smoothly into cells within the computation domain, where ε is a constant to adjust the strength of function, and ξ is the distance between cell center and the center of segments on the actuator line. The selection of ε value is proposed by Shives *et al.* [33]. In this paper, $\varepsilon = 4$ is chosen for better predictions of the wake profile and aerodynamic loadings. The distributed forces $\vec{F}_\varepsilon$ induced by an individual blade on each cell can thus be calculated by the convolution of $\vec{F}_{2D}$ and the Gaussian weight function

$$\vec{F}_\varepsilon = \vec{F}_{2D} \otimes \eta_\varepsilon. \tag{2.11}$$

For a turbine with N blades, the distributed forces are:

$$\vec{F}_\varepsilon = \sum_{i=1}^{N} \int_0^R \vec{F}_{2D} \cdot \eta_\varepsilon(\xi) dr \tag{2.12}$$

In the following three subsections, three methods to determine the relative velocity between the turbine blade and incoming wind (iterative process in BEM, LVS and LEI), which are crucial for the accuracy of $\vec{F}_{2D}$, are compared.

2.2.1 Iterative Process in BEM

The principle of BEM is shown in figure 2.1, where X is the streamwise direction, and θ is the tangential (rotational) direction. For a wind turbine blade rotating at an angular velocity Ω and exposed to wind with incoming velocity of U_∞. At the radial (spanwise) element with radius r, the relative velocity U_{rel} between the rotating blade element and incoming wind is

$$U_{rel}^2 = [(1+a')\Omega r]^2 + [(1-a)U_\infty]^2 \tag{2.13}$$

where a' is the tangential velocity induction factor and a is the axial velocity induction factor. a and a' can be solved in an iterative process. If one defines ϕ as the angle between $\vec{U_{rel}}$ and the rotor plane:

$$\phi = \tan^{-1}\left(\frac{(1-a)U_\infty}{(1+a')\Omega r}\right), \tag{2.14}$$

the angle of attack is $\alpha = \phi - \beta - \gamma$ where β is the pitch angle and γ is the twist angle. In addition, the lift force and drag force per unit length along the radial direction are

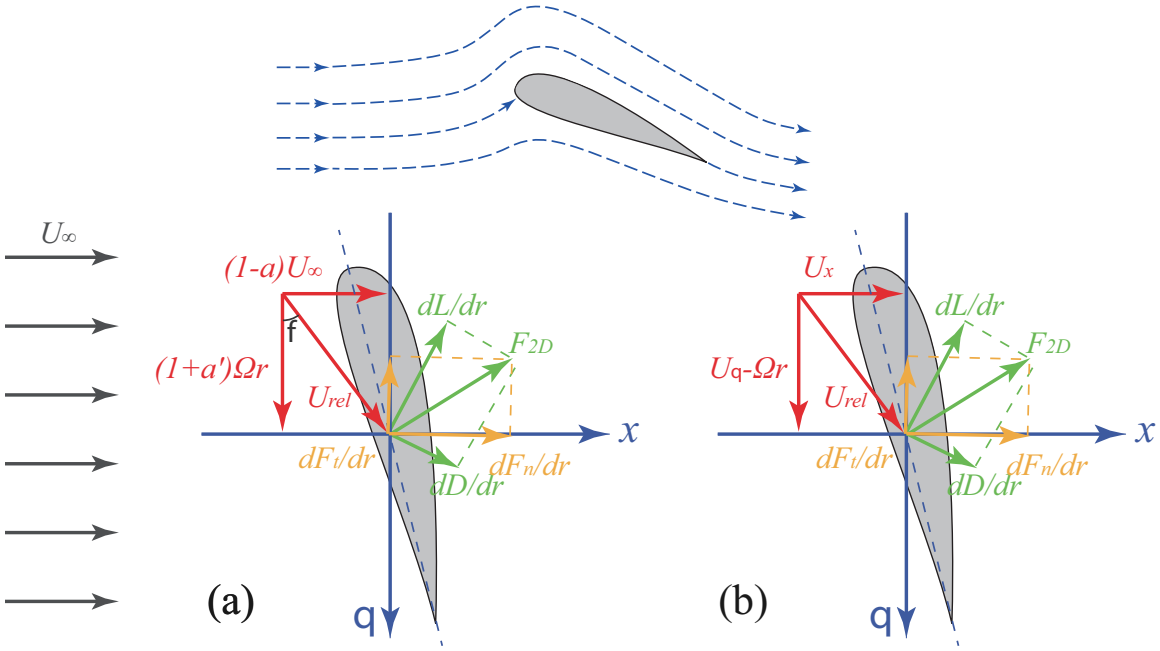

Figure 2.1. Principles of (a) BEM and (b) LVS and LEI.

$$\frac{dL}{dr} = \frac{1}{2}\rho U_{rel}^2 \cdot c \cdot C_l(\alpha, Re), \tag{2.15}$$

$$\frac{dD}{dr} = \frac{1}{2}\rho U_{rel}^2 \cdot c \cdot C_d(\alpha, Re), \tag{2.16}$$

where c is the local chord length and Reynolds Number is defined as $Re = \rho U_{rel} \cdot c/\mu$. Lift coefficient C_l and drag coefficient C_d are obtained from tabulated airfoil characteristics for a given combination of Re and α. The resultant force on all N blades can be decomposed into axial and tangential components:

$$\frac{dF_n}{dr} = N\left(\tfrac{dL}{dr}\cos\phi + \tfrac{dD}{dr}\sin\phi\right), \tag{2.17}$$

$$\frac{dF_t}{dr} = N\left(\tfrac{dL}{dr}\sin\phi - \tfrac{dD}{dr}\cos\phi\right). \tag{2.18}$$

One can define $C_N(Re, \alpha)$ and $C_T(Re, \alpha)$ as

$$C_N = N(C_l\cos\phi + C_d\sin\phi), \tag{2.19}$$

$$C_T = N(C_l\sin\phi - C_d\cos\phi). \tag{2.20}$$

and thus

$$\frac{dF_n}{dr} = \tfrac{1}{2}\rho U_{rel}^2 \cdot c \cdot C_N(\alpha, Re), \tag{2.21}$$

$$\frac{dF_t}{dr} = \tfrac{1}{2}\rho U_{rel}^2 \cdot c \cdot C_T(\alpha, Re). \tag{2.22}$$

dF_n/dr and dF_t/dr can also be obtained from momentum theory and angular momentum theory [22],

$$\frac{dF_n}{dr} = \quad 4a(1-a)\pi\rho {U_\infty}^2 r \tag{2.23}$$

$$\frac{dF_t}{dr} = \quad 4a'(1-a)\pi\rho U_\infty r^2\Omega. \tag{2.24}$$

From Equations (2.17) to (2.24), one may have

$$\frac{1}{2}\rho U_{rel}^2 \cdot c \cdot C_N = \quad 4a(1-a)\pi\rho {U_\infty}^2 r, \tag{2.25}$$

$$\frac{1}{2}\rho U_{rel}^2 \cdot c \cdot C_T = \quad 4a'(1-a)\pi\rho U_\infty r^2\Omega. \tag{2.26}$$

From Equations (2.25) and (2.26) we can get a pair of new values of the induction factors (a_{new} and a'_{new}):

$$2a_{\text{new}}(1-a_{\text{new}}) = \frac{\sigma}{4\sin^2\phi}C_N, \tag{2.27}$$

$$2a'_{\text{new}}(1-a_{\text{new}}) = \frac{\sigma}{4\sin\phi\cos\phi}C_T, \tag{2.28}$$

where $\sigma = Nc/2\pi r$. In BEM, the rotor plane is assumed to be a permeable disk. To account for the physical difference between the permeable disk and the finite blades

of a turbine rotor disk, tip loss corrections are usually adopted into Equations (2.27) and (2.28):

$$\frac{a_{\text{new}}F(1-a_{\text{new}}F)}{(1-a_{\text{new}})^2} = \frac{\sigma}{4\sin^2\phi}C_N F_1, \tag{2.29}$$

$$\frac{a'_{\text{new}}F(1-a_{\text{new}}F)}{(1-a'_{\text{new}})(1-a_{\text{new}})} = \frac{\sigma}{4\sin\phi\cos\phi}C_T F_1, \tag{2.30}$$

where functions F_1 [43, 44] and F [22] are:

$$F_1 = \frac{2}{\pi}\cos^{-1}\left[\exp\left(-g\frac{N(R-r)}{2r\sin\phi}\right)\right], \tag{2.31}$$

$$F = \frac{2}{\pi}\cos^{-1}\left[\exp\left(-\frac{N(R-r)}{2r\sin\phi}\right)\right]. \tag{2.32}$$

Here R is the blade length and

$$g = \exp\left[-0.125\left(\frac{N\Omega R}{U_\infty} - 21\right)\right] + 0.1. \tag{2.33}$$

More details about the tip-loss corrections can be found in [43, 44]. Solving 2.29 and 2.30, one has

$$a_{\text{new}} = \frac{2 + Y_1 - \sqrt{4Y_1(1-F) + Y_1^2}}{2(1+FY_1)}, \tag{2.34}$$

$$a'_{\text{new}} = \frac{1}{(1-a_{\text{new}}F)Y_2/(1-a) - 1}, \tag{2.35}$$

in which

$$Y_1 = \frac{4F \sin^2 \phi}{\sigma F_1 C_N}, \tag{2.36}$$

$$Y_2 = \frac{4F \sin \phi \cos \phi}{\sigma F_1 C_T}. \tag{2.37}$$

The iterative process in BEM starts with adopting a pair of initial guess values for a and a'. Then angle of attack α, C_l, and C_d, can be calculated. A new pair of a and a' can be calculated from Equations (2.34) and (2.35). This iterative process continues until the values for a and a' converge. The resultant force applied on each spanwise section is thus

$$\vec{F}_{2D} = cN\frac{1}{2}\rho U_{rel}^2 \left(C_N \vec{n} + C_T \vec{t}\right) F_1. \tag{2.38}$$

2.2.2 Local Velocity Sampling (LVS)

LVS samples the velocity directly at the center of the segment on the actuator line, as shown in figure 2.2. In this method, the relative velocity is expressed as follows

$$U_{rel}^2 = U_x^2 + (U_\theta - \Omega r)^2 \tag{2.39}$$

where U_x is the axial component of the sampled velocity and U_θ is the tangential component. In LVS, a combination of F_1 correction [44] and Prandtl's correction [22] are also adopted. According to Shen *et al.* [44], F_1 correction shows a good prediction in the thrust coefficient, but no results about power output are presented. Jha *et*

al. [14] shows that the selection of $\varepsilon = 4$ will lead to an overprediction of power output, and the application of Prandtl's factor to tangential force will reduce the power output. In this paper, the following resultant force is applied on each spanwise section in the LES-ALM solver:

$$\vec{F_{2D}} = cN\frac{1}{2}\rho U_{rel}^2 \left(F_1 C_N \vec{n} + F C_T \vec{t}\right). \tag{2.40}$$

C_N and C_T are determined in the same way as the process as in BEM, except that the relative velocity is sampled directly from the flow field and no iteration process is needed.

2.2.3 Lagrange Euler Interpolation (LEI)

In ALM, the actuator lines are built in Lagrangian point of view, and the background domain is built in Eulerian point of view, so the velocities on segments of actuator lines can be interpolated from the background in LEI, as shown in figure 2.2-b:

$$\vec{U}(\vec{X}) = \sum_i \vec{U}(\vec{x})\delta_h(\vec{x} - \vec{X})V(\vec{x}), \tag{2.41}$$

using a discrete delta function

$$\delta_h(\vec{x} - \vec{X}) = \frac{1}{\delta^3}\phi\left(\frac{x - X}{\delta}\right) \cdot \phi\left(\frac{y - Y}{\delta}\right) \cdot \phi\left(\frac{z - Z}{\delta}\right) \tag{2.42}$$

Here i indicates each computation cell to be collected, δ the dimension of this cell, $\vec{x}$ the coordinate of that cell, and $\vec{X}$ the coordinate of the center of actuator line segments. $V(\vec{x})$ is the cell volume, ϕ is a delta function. In this work, a smoothed discrete three-point delta function developed by Yang *et al.* [45] is adopted:

$$\phi(s) = \begin{cases} \frac{17}{48} + \frac{\sqrt{3}\pi}{108} + \frac{|s|}{4} - \frac{s^2}{4}\frac{1-2|s|}{16}\sqrt{-12s^2+12|s|+1} \\ \quad -\frac{\sqrt{3}}{12}\sin^{-1}\left(\frac{\sqrt{3}}{12}(2|s|-1)\right) \quad \text{if} \quad |s| \le 1 \\ \frac{55}{48} - \frac{\sqrt{3}\pi}{108} - \frac{13|s|}{12} + \frac{s^2}{4}\frac{2|s|-3}{48}\sqrt{-12s^2+36|s|-23} \\ \quad +\frac{\sqrt{3}}{36}\sin^{-1}\left(\frac{\sqrt{3}}{12}(2|s|-3)\right) \quad \text{if} \quad 1 < |s| \le 2 \\ 0 \qquad \text{if} \quad 2 \le |s| \end{cases} . \tag{2.43}$$

where s represents $\frac{x-X}{\delta}$, $\frac{y-Y}{\delta}$ and $\frac{z-Z}{\delta}$. $\vec{U}(\vec{X})$ can also be decomposed into U_x and U_θ. Equation (2.39) can be adopted to determine U_{rel}. Equation (2.40) can then be used to compute $\vec{F}_{2D}$.

2.3 Important Parameters in ALM

After showing all the details about ALM, it is time to discuss the most important parameters influencing the accuracy of ALM. In Equation (2.11), one can figure out that the body forces distributed in each cell are contributed by two parts. The first one is the Gaussian Weight Function, while the second one is the line forces generated

by BEM. In Gaussian Weight Function Equation (2.10), ξ is fixed for a given case, so the value of ε is the vital part for the accuracy of Gaussian Weight Function. Many researches have been carried out to investigate how to choose ε. There are three approaches to determine ε: (1) Gird-Based Radius [24, 25], $\varepsilon/\Delta = const$, (2) Chord-Based Radius [33], $\varepsilon/c = const$, (3) Elliptic Gaussian Radius [14]. Equations (2.15) and (2.16) show the line forces generated by BEM. One can see that U_{rel}, C_l and C_d are the unfixed factors. In these three factors, U_{rel} is the most important one, because its magnitude determines Re and its components determine AOA. Re and AOA further determine C_l and C_d. From this analysis, one can conclude that the accuracy of ALM should be very sensitive to U_{rel}. The main task of this work is to evaluate different ways of obtaining U_{rel} and to test its performance on large wind farm projects.

2.4 Turbulent Inlet Conditions

In this paper, a turbulent inlet boundary condition is applied to the simulation, coupled with the ABL profile. The inlet turbulence is generated by a vortex method, which was put forward by Sergent [40], and then implemented by Mathey *et al.* [41]. The vortex method is more efficient than Synthesized turbulence methods [35,36] and precursor simulation methods [37, 38] in terms of computational cost. More details about the other two methods can be found in reviews [46, 47]. In vortex method, velocity fluctuation is added to the mean flow by a 2D fluctuating vorticity field in an

inlet plane normal to the streamwise direction. In Lagrangian frame, the transport of vorticity of incompressible flow is described by

$$\frac{d\omega}{dt} = \omega \cdot \nabla u + \nu \nabla^2 \omega. \tag{2.44}$$

The vorticity at a position $\vec{x}$ can be calculated by adding the contribution of all the vortex points

$$\omega(\vec{x}, t) = \sum_{i}^{M} \Gamma_i(\vec{x_i}) \eta(\mid \vec{x} - \vec{x_i} \mid, t) \tag{2.45}$$

where Γ_i is the circulation, M is the number of vortices and η is the assumed spatial distribution of vortex. Γ_i, which represents the intensity of turbulence, is a function of local turbulent kinetic energy (TKE) k:

$$\Gamma_i(\vec{x_i}) = 4\sqrt{\frac{\pi S k(\vec{x_i})}{3M(2\ln(3) - 3\ln(2))}}, \tag{2.46}$$

where S is the area of inlet boundary. The spatial distribution of η is given by

$$\begin{aligned} \eta(\mid \vec{x} - \vec{x_i} \mid) &= \frac{1}{2\pi\iota^2}\left[2\exp\left(-\frac{\mid \vec{x} - \vec{x_i} \mid^2}{2\iota^2}\right) - 1\right] \\ &\quad \cdot 2\exp\left(-\frac{\mid \vec{x} - \vec{x_i} \mid^2}{2\iota^2}\right), \end{aligned} \tag{2.47}$$

where ι is the size of the vortex, which is bounded by the local grid size Δ. This can keep the vortex in the resolvable scale of LES. The size ι can be determined from local TKE and dissipation rate ς

$$\iota = m \cdot k^{1.5}/\varsigma \tag{2.48}$$

where m is set to 0.08. The resulting tangential velocity fluctuation can be obtained by using Biot-Savart law which relates the synthetic in-plane velocity fluctuation to the vorticity

$$\begin{aligned} \vec{u}(\vec{x}) &= (0, v', w') \\ &= \frac{1}{2\pi}\sum_{i}^{M}\Gamma_i \frac{(\vec{x}-\vec{x_i})\times\vec{n}}{(\mid \vec{x}-\vec{x_i} \mid)^2}\cdot\left[1-\exp\left(-\frac{\mid \vec{x}-\vec{x_i} \mid^2}{2\iota^2}\right)\right] \\ &\quad \cdot\exp\left(-\frac{\mid \vec{x}-\vec{x_i} \mid^2}{2\iota^2}\right). \end{aligned} \tag{2.49}$$

where $\vec{n}$ is the unit vector in axial/streamwise direction.

By far, vortex method can only generate velocity fluctuation in a plane normal to the streamwise direction. A simplified linear kinematic model (LKM) is used to generate streamwise velocity fluctuation [41]. In LKM, the streamwise velocity fluctuation u' can be related to tangential velocity fluctuation by

$$u' = -\vec{u}(\vec{x})\cdot\vec{g} \tag{2.50}$$

where $\vec{g}$ is the unit vector of mean velocity gradient. In the present study, vortex method is coded into OpenFOAM.

The LES-ALM solver with vortex method implemented into OpenFOAM adopts PISO algorithm. During time marching, the solver exports the global continuity error for the last corrector step in the PISO loop. This non-dimensional error is at the order of 10^{-11} for the whole domain, which ensures the continuity is satisfied. In OpenFOAM, the non-dimensional error is computed like this:

$$GlobalError = \Delta t \cdot \bigtriangledown \cdot u, \tag{2.51}$$

where Δt is the time step. To calculate the divergence of u, u is first interpolated from cell center to cell surface; then do the surface summation for u; then the surface summation of u is divided by the volume of the cell. Actually, the global summation of surface summation of u for individual cell multiplied by the density of air and time step is the continuity error for the whole domain, so $GlobalError \times \triangle V = GlobalMassError$. The cell length adopted in this work is 0.5m or 0.25m, so the global mass continuity error is at the order of 10^{-12} kg or 10^{-13} kg per time step.

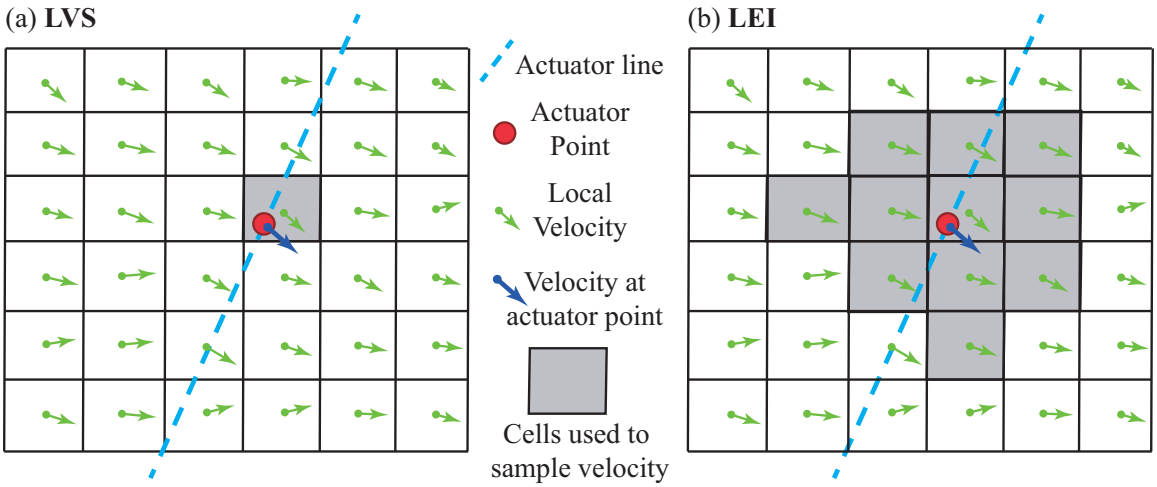

Figure 2.2. Schematics of LVS and LEI.

3. DESCRIPTIONS OF SIMULATIONS

3.1 OpenFOAM Framework

In this work, pisoFoam solver in OpenFOAM is modified, and ALM with LEI, LVS and iterative BEM process are incorporated into the solver. A turbulent inlet boundary condition base on vortex method is also implemented in OpenFOAM. All the computations in this work are made possible by carter cluster in Purdue University. Carter consists of HP compute nodes with two 8-core Intel Xeon-E5 processors (16 processors per node) and 32 GB of memory. The test case uses 2 nodes, while all other cases use 12 nodes. In this work, we use the numerical solver in OpenFOAM 2.2.1 [48] to solve Equations (2.3) and (2.4) with Smagorinsky model. The filtered Navier-Stokes equations with bodyforce are discretized with an unstructured collocated finite-volume formulation. The velocity fluxes are constructed with Rhie-Chow interpolation [49]. All other interpolations are either linear (second-order central differencing) or filtered linear (second-order central differencing with a small amount of upwinding) [48]. Time advancement uses PISO (Pressure-Implicit Splitting Operation) algorithm [50] with one predictor step and three correction steps. The momentum equations are solved with diagonal incomplete LU (DILU) pre-conditioned biconjugate-gradient (PBiCG) solver in the predictor step. The pressure equation is solved in the corrector steps with generalised geometric-algebraic multi-grid (GAMG)

solver with a Gauss-Seidel smoother to reduce computational cost. For the stand alone turbine case, all the side walls are set to be slip; and the outlet boundary is set to be zeroGradient. For wind farm cases simulated in this thesis, the boundary conditions are the same, except inlet boundary, which will be presented in each case. The top wall is set to be symmetryPlane; the side walls are set to be cyclic; the bottom wall is set to be non-slip wall; and the outlet boundary is set to be zeroGradient. Near wall treatment near the bottom wall is ignored, because what we care about is the flow field at the height where turbine exists, which are far above the bottom wall. For all the cases simulated, x denotes the streamwise direction, y denotes the horizontal direction and z denotes the vertical direction. All the cells in this thesis is cubic, which means the grid lengths are equal in both x, y, and z directions.

3.2 Test Case: NREL Phase VI Wind Turbine

An experimental study on a two-blade NREL Phase VI with S809 airfoil has been conducted in NASA Ames wind tunnel [5]. A recent LES study of the near wake and aerodynamic loading of this turbine is reported in Ref. [20] using the exact 3D blade geometries. In this paper, the aerodynamic loadings of the aforementioned LES-ALM methods are validated by the experiment results, and the wake by the simulation results. The values for C_l and C_d are interpolated from the data provided in [4]. The computational domain is presented in figure 3.1, with a streamwise length of $L_x = 55.3$ m, a width of $L_y = 36.6$ m, and a height $L_z = 24.4$ m. The diameter of NREL Phase VI turbine is D=10.06 m. The mesh for this case is structural with a

grid number of $N_x \times N_y \times N_z = 214 \times 147 \times 98 = 3,082,884$. The turbine is placed 12.2 m above the ground (hub height), and $2D$ behind the inlet boundary. A uniform incoming wind speed of 7 m/s is adopted, identical to the experimental condition generated in the wind tunnel. The wind turbine rotates at 72 rpm. The origin of the coordinate is set at the turbine hub. In this case, the effect of nacelle and tower is not considered. The cell length is chosen to be 0.25 m ($\Delta/D = 1/40$), and $\Delta_b/\Delta = 1.5$, as suggested in Ref. [14], where Δ is the grid size, and Δ_b is the length of each segment in the actuator line. The time step is set to be 0.01s (83 time steps per circle). In this case, results of different methods to obtain relative velocity are compared to identify the best performed method for unsteady LES-ALM simulation on wind farm.

3.3 Simulated Atmospheric Boundary Layer

The wind turbine array is exposed to a simulated atmospheric boundary layer (ABL). The mean streamwise velocity is represented by a power law profile [20].

$$u(z) = U_{\text{hub}} \left(\frac{z - z_{\text{ground}}}{z_{\text{hub}} - z_{\text{ground}}} \right)^{0.35} \tag{3.1}$$

where U_{hub} characterizes the wind speed at hub height, z_{ground} the ground height, and z_{hub} the hub height. In the present work, U_{hub} is set to be 7 m/s. The velocity profile

generated by the power law is shown in figure 3.2. The friction velocity u^* can be obtained by the logarithmic law [51, 52].

$$u^* = U_{\text{hub}}\kappa / \ln\left(\frac{z_{\text{hub}} - z_{\text{ground}} + z_0}{z_0}\right) \tag{3.2}$$

where $\kappa = 0.4$ is the von Karman constant, z_0 roughness length (set to 0.1 m in this paper), and u^* the friction velocity. By matching the ABL profile (Equation (3.1)) with the logarithmic profile (Equation (3.2)) at hub height, the value of u^* can be determined. Furthermore, local turbulent kinetic energy (TKE) k and dissipation rate ς are related to u^* according to [53]

$$k = u^{*2}/0.3 \tag{3.3}$$

$$\varsigma(z) = \frac{u^{*3}}{\kappa(z - z_{\text{ground}} + z_0)} \tag{3.4}$$

k and ς are then used to generate the synthetic turbulent conditions at the inlet of the computation domain, as detailed in section 2.4.

3.4 A Small Wind Farm in Full Wake Setting

A numerical study on five NREL Phase VI wind turbines deployed in full wake setting is presented to show the potential of the LES-ALM solver in Open FOAM with LEI, as shown in figure 3.3, with a streamwise length $L_x = 260$ m, width $L_y =$ 24.4 m, and height $L_z = 24.4$ m. The grid number of this case is $N_x \times N_y \times N_z =$

$1041 \times 98 \times 98 = 9,997,764$. Each turbine is placed 12.2 m above the ground. The first row is $1D$ behind the inlet boundary. The distances between two turbines are $5D$ in both streamwise direction and horizontal direction. The mean incoming flow is generated based on Equation (3.1). The turbulent velocity fluctuation is added to the mean flow based on the vortex method described in 2.4. Each wind turbine rotates at 72 rpm. The origin of the coordinate is set at the center of the inlet boundary. The cell length is also chosen to be $0.25m$ ($\Delta/D = 1/40$), and $\Delta_b/\Delta = 1.5$. The time step is set to be 0.01s (83 time steps per circle).

3.5 A Wind Farm Under Different Inflow Angle

In this work, a small wind farm composed of 25 (5×5) wind turbines are simulated under different inflow angles from full wake setting to partial wake settings. Five inflow angles (0^o, 5^o, 15^o, 30^o and 45^o) are tested. The computational domain is presented in figure 3.4, with a height $L_z = 24m$ for all the inflow angles. The cell length is set to be 0.5m ($D/\Delta = 20$). In the full wake setting case, the domain has a length $L_x = 250m$ and a width $L_y = 250m$ so the grid number for this case is $N_x \times N_y \times N_z = 501 \times 501 \times 49 = 12,299,049$. Under 5^o and 15^o inflow angle, the domain has a length $L_x = 280m$ and a width $L_y = 280m$, and its total grid number is $N_x \times N_y \times N_z = 561 \times 561 \times 49 = 15,421,329$. For 30^o inflow angle, the length L_x and L_y are both 310 m, so it has a grid number of $N_x \times N_y \times N_z = 621 \times 621 \times 49 = 18,896,409$. For 45^o inflow angle, the length L_x and L_y are both $320m$, so its grid number is $N_x \times N_y \times N_z = 641 \times 641 \times 49 = 20,133,169$. As shown in figure 3.4, each turbine in

the farm is labeled as T_{ij}, where i indicates column index, and j indicates row index. The diameter of NREL Phase VI turbine is $D = 10.06$ m. The turbines are placed $12m$ above the ground. For all the five inflow angles, the hub of first row is $1D$ behind the coordinate origin which is placed within the inlet boundary. The distance between two adjacent turbines in the same row/column is $5D$ in both streamwise direction and horizontal direction. The inlet velocity is generated in the same way as described in 3.4. The wind turbine rotates at 72 rpm. The effect of tower is not considered. The velocity field under different inflow angles will be analyzed, and the distributions of power output and thrust coefficients will also be presented and compared. The time step is also set to be 0.01s (83 time steps per circle).

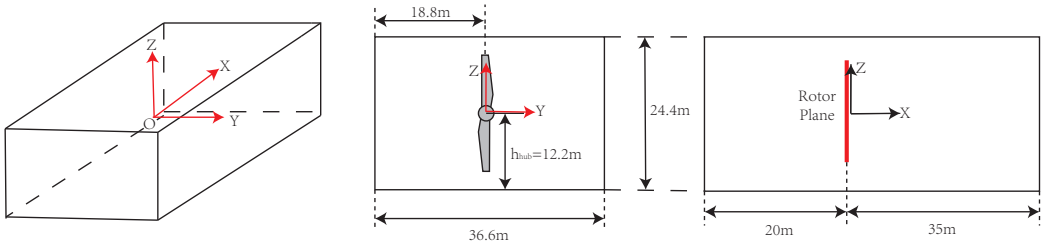

Figure 3.1. Computational domain of NREL Phase VI wind turbine case.

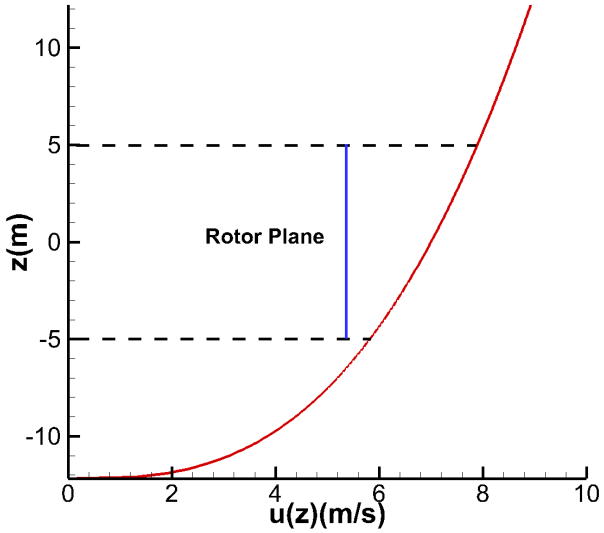

Figure 3.2. ABL velocity profile generated by power law.

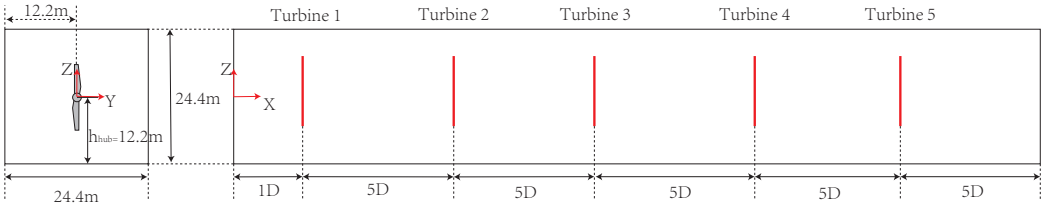

Figure 3.3. Computational domain of the simulation of wind farm in full wake setting.

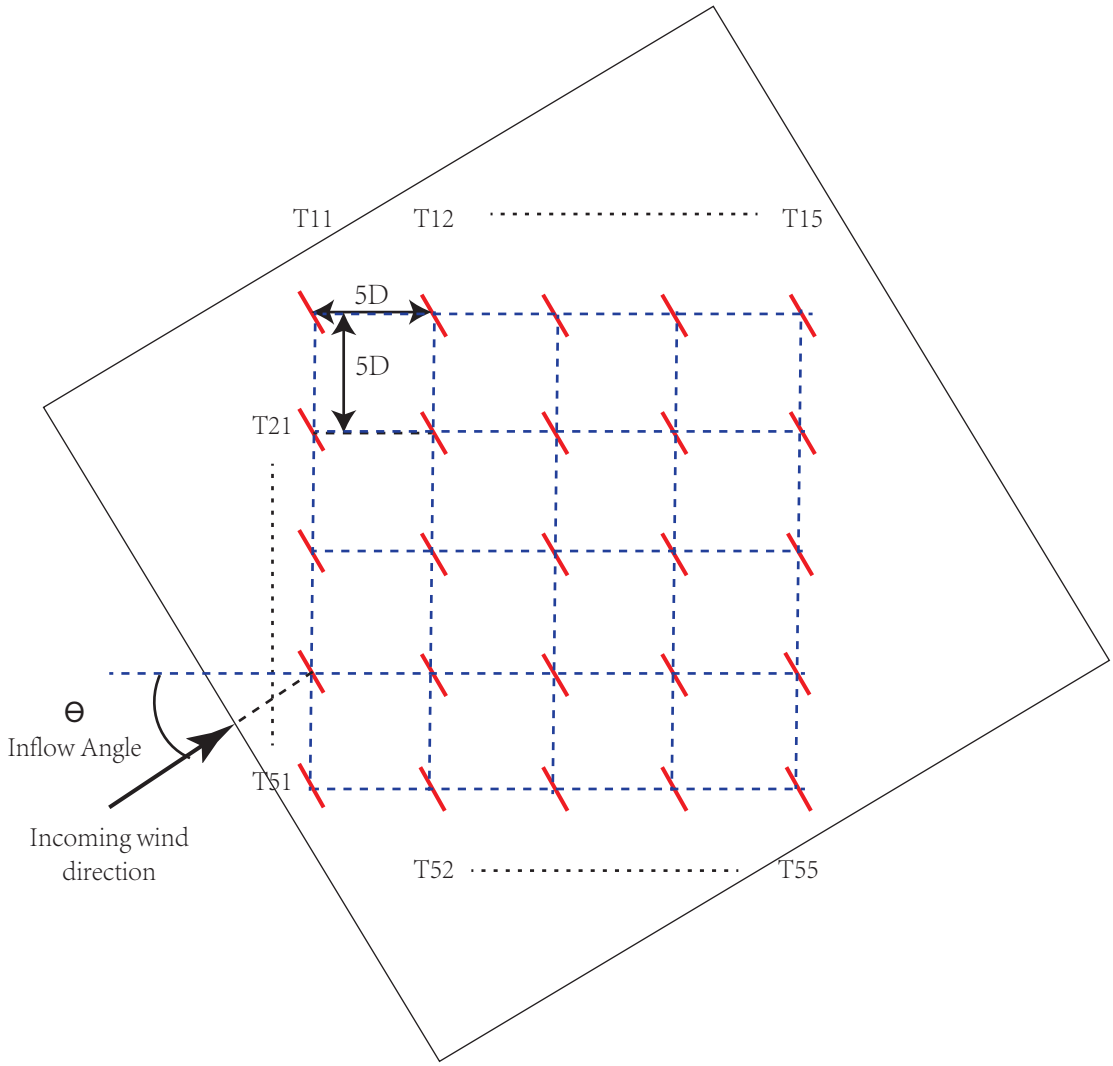

Figure 3.4. Illustration of wind farm under inflow angle.

4. RESULTS

4.1 Overview

For the first case in this section, BEM, LVS and LEI are all tested. BEM is independent of the flow field. In LVS and LEI, the flow solver first samples relative velocity from the flow field generated for the previous time step. Then the relative velocity is used to generate the body forces in ALM. The body forces are then fed into the LES solver to obtain the velocity field for the current time step. For the first time step, the relative velocity is sampled from the initial flow field at $t = 0$. However, the existence of wind turbine is not considered for the initial time step, so there is a transient period for the first several time steps in which the flow field obtained from the solver is not accurate. After the transient period, the effects of wind turbine are fully cooperated into the flow field, the flow field is considered to be accurate. For the test case, both time and phase averaging begins after 833 time steps ($8.33s$, 10 circles) and lasts for another 833 time steps. For the small wind farm in full wake case in this section, LEI is adopted. Time averaging begins after 6000 time steps ($60s$) and lasts for another 1666 time steps (20 circles). For the wind farm under different inflow angles case, time averaging begins after 8000 time steps ($80s$) and lasts for another 1666 time steps (20 circles).

4.2 Test Case

Once the flow field is determined by the LES-ALM, C_N and C_T can be used to analyze the aerodynamic power $\mathbf{P}$ and thrust force $\mathbf{T}$ applied on the turbine:

$$\mathbf{P} = \sum_{i=1}^{I} \frac{1}{2} \rho W^2 C_T c \Delta_b r \Omega, \tag{4.1}$$

$$\mathbf{T} = \sum_{i=1}^{I} \frac{1}{2} \rho W^2 C_N c \Delta_b. \tag{4.2}$$

Table 4.2 comprises the power coefficients and thrust coefficients from different methods, where

$$C_{\mathbf{p}} = \frac{N \cdot \mathbf{P}}{0.5 \rho \pi R^2 U_\infty^3}, \tag{4.3}$$

$$C_{\mathbf{t}} = \frac{N \cdot \mathbf{T}}{0.5 \rho \pi R^2 U_\infty^2}, \tag{4.4}$$

and I is the total number of segments on actuator line. N is the number of turbine blade.

Results in table 4.1 show that BEM, LVS and LEI give reasonable predictions of both power output and thrust, when compared to the experimental values (EXP*) and LES with exact turbine geometry (LES**. This shows the advantage of ALM over LES with geometric details in aerodynamic loading prediction. Even though LES-ALM is superior to geometry-resolved LES in terms of computation cost, it still cannot replace the geometry-resolved method, because ALM is not able to resolve details like blade surface pressure distribution, near wake profile, etc. LEI predicts a

$C_{\mathbf{t}}$ which is 3.7 % larger than the measured value, and a $C_{\mathbf{p}}$ which is 1.4 % smaller. The prediction of BEM (iterative process) is 2.3% larger than the measured $C_{\mathbf{p}}$, and 3.0% smaller than the measured $C_{\mathbf{t}}$. The results of LVS is 5.2% larger than the measured thrust, and 4.5% larger than the measured power. Among the three ALM-type simulations, results from LEI and BEM are better than those from LVS based on the comparison. The predictions from LEI and BEM are similar. LEI is preferred, because it utilizes the flow field obtained by the NS solver, which tunes the low fidelity BEM theory to calculate aerodynamic forces. In particular, it can be applied to study unsteady phenomena, like velocity fluctuation introduced by turbulence, rotor-rotor interaction, rotor-tower interaction, etc. It also avoids the major drawback of the iterative process in conventional BEM. LVS also utilizes the resolved flow field, but it is less accurate from the above comparison.

Figure 4.1 presents the normalized streamwise velocity at different downstream locations. We can see that in far wake (x/D $\geq$ 1), the profiles for LVS are closer to prediction from LES** with exact turbine geometries than those of LEI and iterative BEM process. According to one-dimensional momentum equation, the change of streamwise velocity (velocity deficit) is proportional to the thrust, so the sequence of the four simulations based on the velocity deficit is the same as the sequence based on the thrust: LES** (largest), LVS, LEI and iterative process (smallest). The measured value of thrust is between LEI and iterative process, which means the iterative process underpredicts the velocity deficit, while LES**, LVS and LEI overpredict it, and the actual velocity profile should be between the iterative BEM process and LEI. It can

also be observed that in the near wake region (x/D=0.5), the velocity deficit of LEI is slightly larger than that of LVS, which is different than what is observed in the far wake region. In near wake region (x/D=0.5), the body force distributed from actuator line still exists, so the profile is not so accurate. The distributed body force in near wake region is also a reason for the inadequacy of ALM in predicting near wake velocity profile.

Figure 4.2 shows the normalized horizontal velocity at different downstream locations. The prediction of LES** on the power output is much more accurate than its prediction on thrust, so we can regard the horizontal profiles of this simulation to be accurate. It can be observed that the profiles of LVS and LEI are closer to those of LES** than those of the iterative BEM process, which means LEI and LVS are more accurate in predicting tangential velocity, and the iterative BEM process underestimates the tangential component of wake profiles.

In figures 4.1 and 4.2, there is no significant difference between the tangential velocity profiles and streamwise velocity profiles of LEI and LVS, but LEI is much more accurate than LVS in predicting aerodynamic loading. This difference is introduced by the different ways to sample velocity from flow field. In figure 4.3, compared are angle of attack (AOA), relative velocity between blade and incoming wind and thrust per unit span of LVS, LEI and the iterative process. The velocity magnitudes between blade and incoming speed are similar among these three methods, but the ratio of the axial velocity component and tangential velocity component, which contributes to the value of AOA, is quite different. This means different ways to sample velocity from

the computational domain have significant influence on different components of the relative velocity. The difference in AOA will lead to a difference in C_N and C_T, which will result in the difference of the final prediction of aerodynamic loadings. LVS overestimates AOA, which leads to a relatively inaccurate prediction of the thrust and power output compared with LEI. It can also be observed that LEI fits better with the experimental spanwise thrust distribution, while LVS clearly overpredicts the distribution, and the iterative process underpredicts this distribution.

Figure 4.4 shows the time averaged streamwise velocity in the central $x - z$ plane ($y = 0$) obtained by LEI. For streamwise velocity, we can observe velocity deficit immediately behind the rotor plane, and the contour is highly symmetric, which is similar to the results reported in [20, 32]. The distributions of time averaged vertical velocity and horizontal velocity behind the rotor plane are quite similar, so only the contours at plane $x/D = 2$ are presented in figure 4.5. In this figure, one can observe that the time averaged vertical velocity and horizontal velocity components are in the counter direction of the turbine rotation, which is the same as observed in [54]. In this stand alone turbine case, we can observe obvious velocity deficit in the wake region, but wake recovery is not so obvious because of the absence of turbulence. Turbulence can enhance mixing effects, hence can bring relatively obvious wake recovery. In the next case, we will adopt vortex method to generate inflow turbulence and analyze wake recovery by LEI.

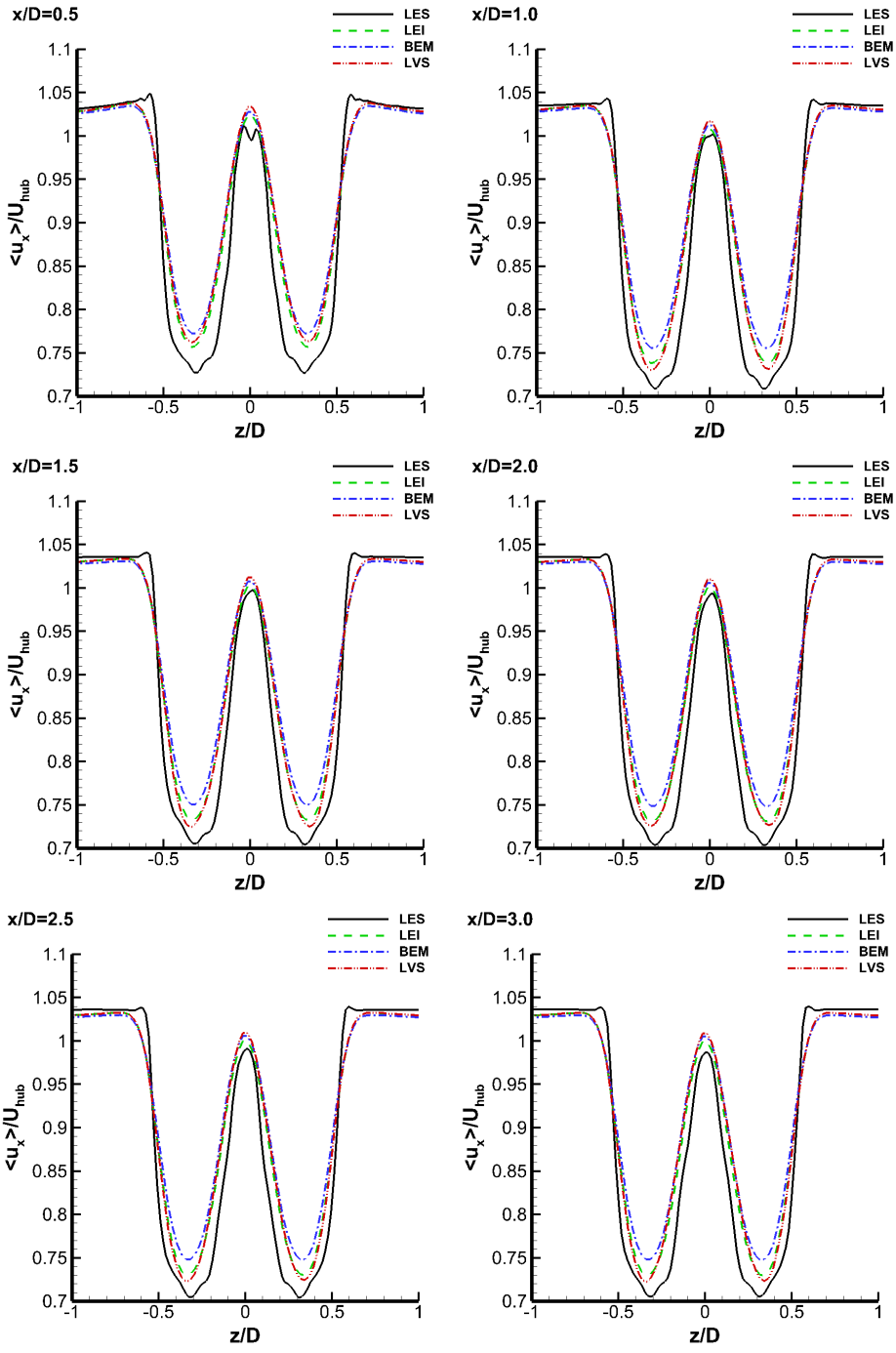

Figure 4.1. Normalized streamwise mean velocity at different downstream locations.

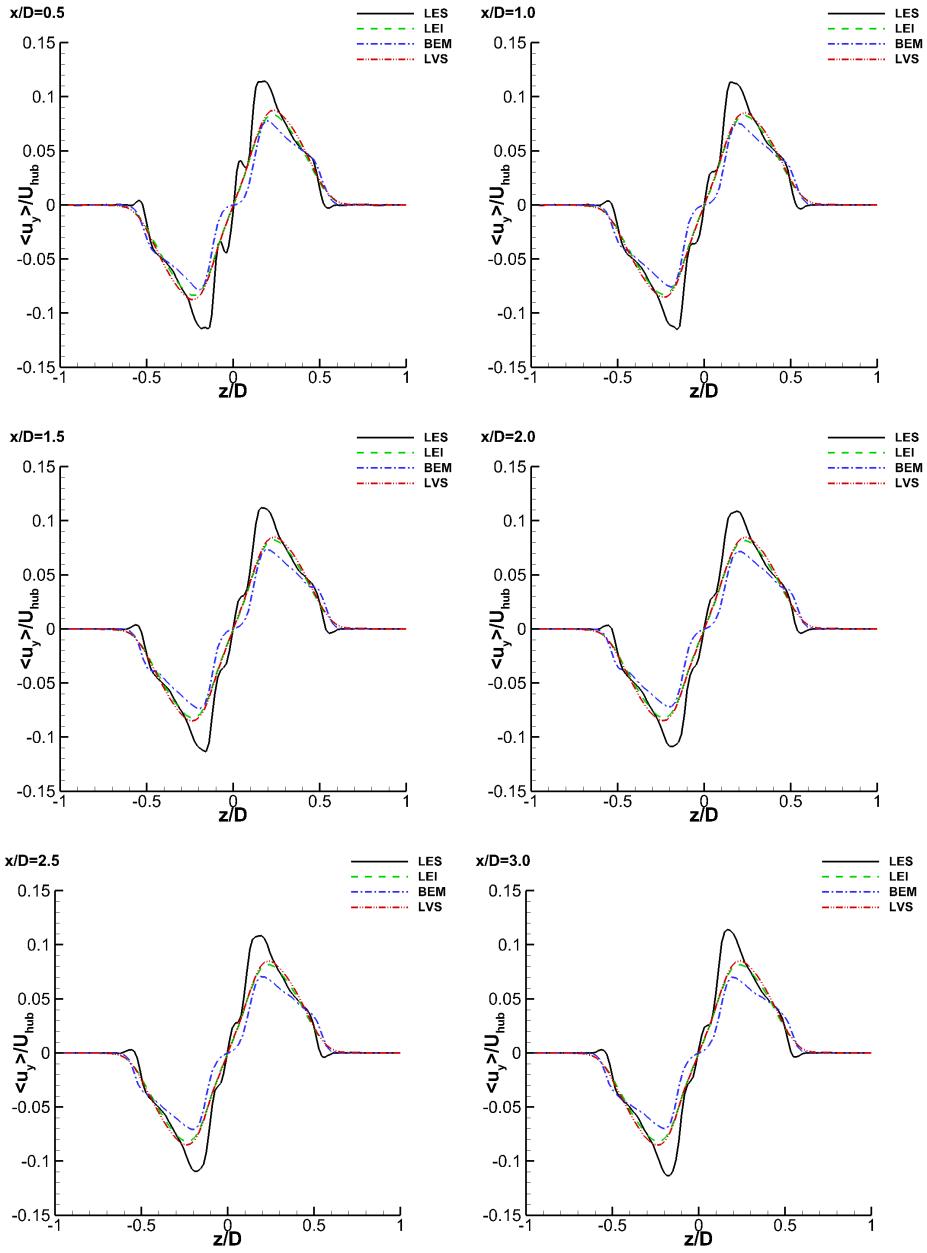

Figure 4.2. Normalized horizontal mean velocity at different downstream locations.

Table 4.1. Comparison of aerodynamic power and thrust using different methods.

Method	BEM	LVS	LEI	Exp*	LES**
$C_{\mathbf{P}}$	0.363	0.371	0.350	0.355	0.333
$C_{\mathbf{T}}$	0.448	0.486	0.479	0.462	0.513

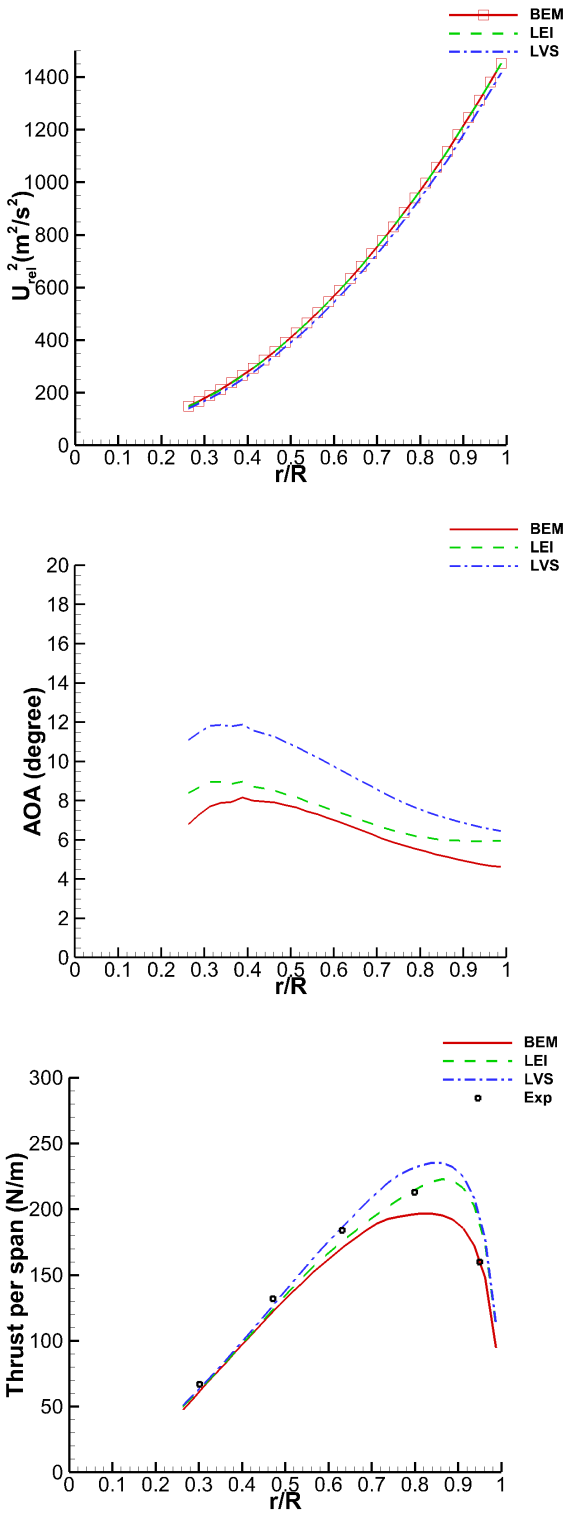

Figure 4.3. Comparison of predicted AOA, thrust per unit span and relative velocity from different methods.

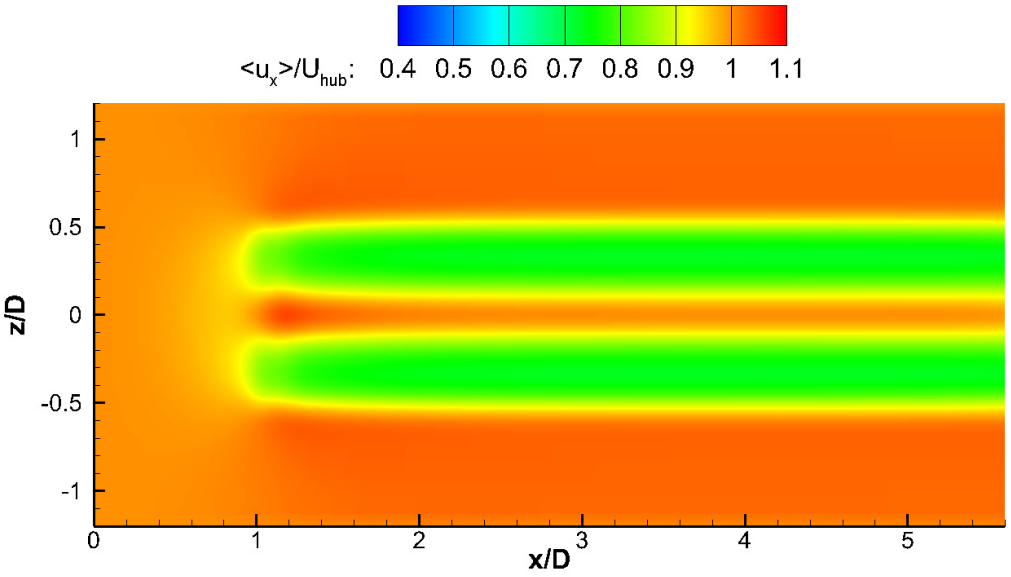

Figure 4.4. Contour of time averaged streamwise velocity in LEI at y=0.

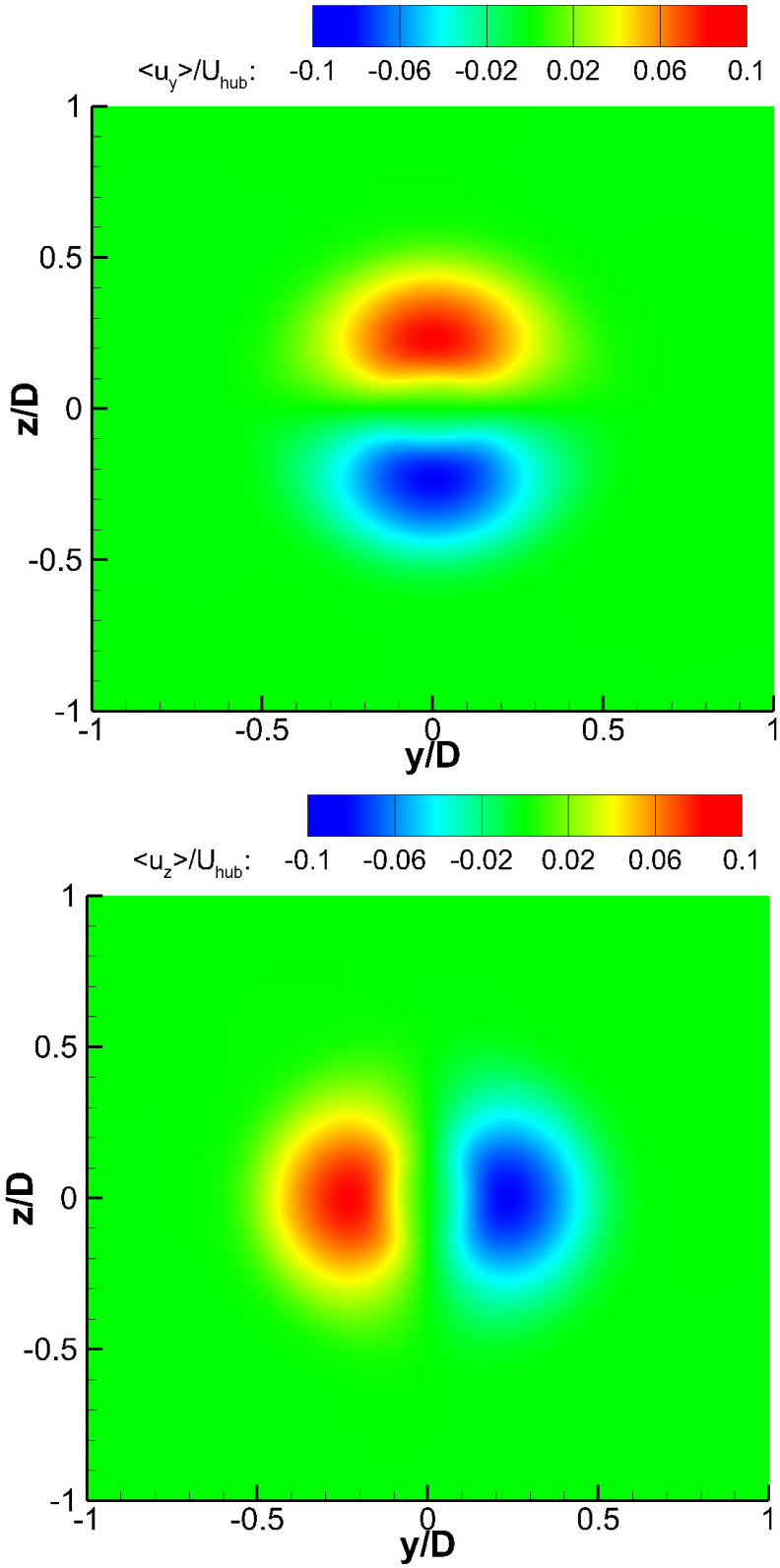

Figure 4.5. Contour of time averaged horizontal and vertical velocity in LEI at x/D=2.

4.3 A Small Wind Farm in Full Wake Setting

Figure 4.6 shows the contours of three components of velocity generated by vortex method at the inlet boundary. The velocity fluctuations brought by turbulence can be observed clearly. Figure 4.7 shows the mean velocity contour at $y = 0$ plane. Wake recovery is observed behind each turbine, which is absent in the stand alone turbine case. In figure 4.8, the mean velocity profile is extracted from lines intersected by plane $y = 0$ and plane $z/D = -0.4$ and by plane $y = 0$ and plane $z/D = 0.4$. In this figure, the black lines represent rotor planes. In both profiles, wind speed drops steeply when it passes the rotor plane. Then the velocity is observed to increase between every two turbines.

Figure 4.9 shows the power and thrust coefficients of the five turbines normalized by the coefficients of the first turbine. The power outputs of the second, third, fourth and fifth turbines are 67%, 52%, 53% and 55% of the first turbine, respectively. The thrust coefficients of the the second, third, fourth and fifth turbines are 79%, 65%, 66% and 68% of the first turbine, respectively. The trends obtained in this work is similar to the trends reported in [55]. In both work, it can be observed that for the power coefficient, there is a steep decrease from the first turbine to the third turbine, but there is no big difference from the third turbine to the fifth turbine. The same tendency is also observed in the plot for thrust coefficient. This means the wake recovery becomes more and more obvious as the wind goes downstream, which is the

same as what is observed in figure 4.8. Wake recovery can also prevent the power output of the downstream turbines from being too low.

The turbulence induced wake recovery can help downstream turbines generate more power, but it will also bring aerodynamic loading fluctuations. In figure 4.10, phase averaged power and thrust coefficients of the first, third and fifth turbines are compared, with their rms values also shown. The maximum rms values of power coefficients for the first, third and fifth turbines are 0.013, 0.052 and 0.061, respectively. The maximum rms of thrust coefficients are 0.012, 0.028 and 0.068, respectively. Power coefficient becomes smaller as the position goes downstream, but the fluctuations become more apparent. The power coefficient is proportional to torque generated by the wind turbine. This means the torque fluctuations are more apparent. The same trend can be observed for thrust coefficient. The turbulence induced aerodynamic loading fluctuations are more and more obvious as the position goes downstream.

4.4 Wind Farm Under Different Inflow Angles

Figure 4.11 shows the normalized mean streamwise velocity at plane $z = 0$. The streamwise velocity is along $x+$ direction. The black lines in the contour represent rotor planes. We can observe velocity deficit behind each rotor plane. The wake of each column is quite similar in the contour, but they are not exactly the same. We can confirm this later when we analyze the power coefficients and thrust coefficients of each turbine in the wind farm. Figure 4.11 shows the normalized mean vertical velocity

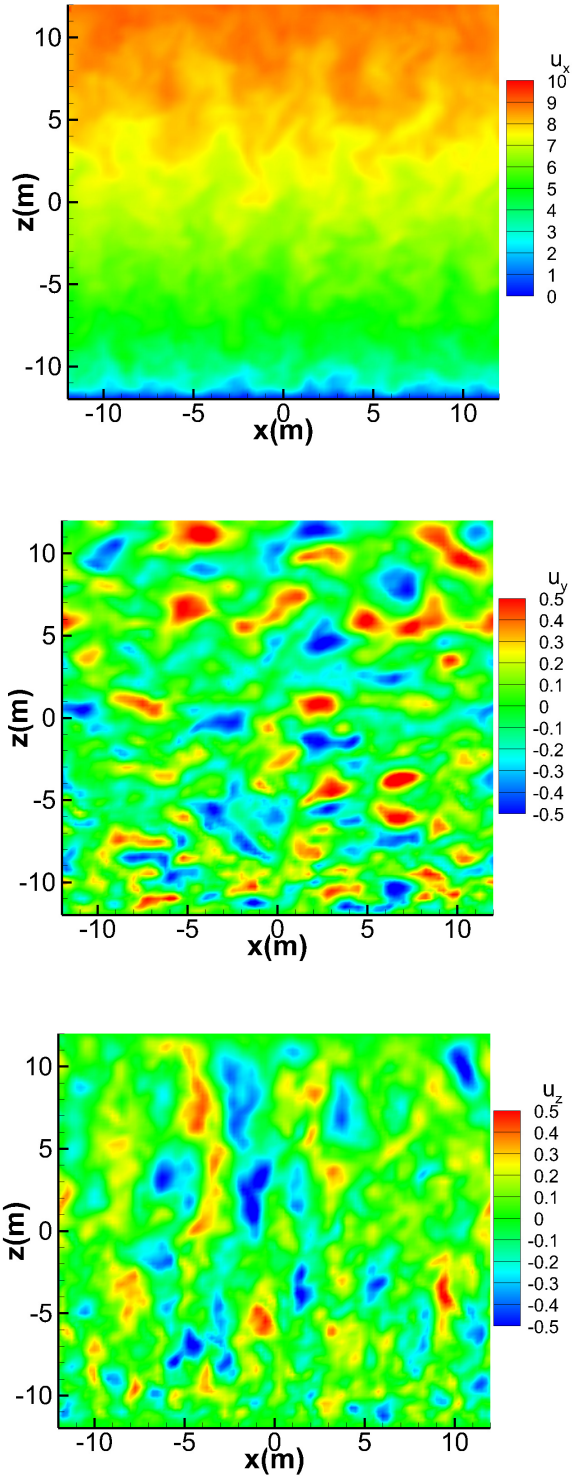

Figure 4.6. A snapshot of velocity contour generated by vortex method at inlet boundary.

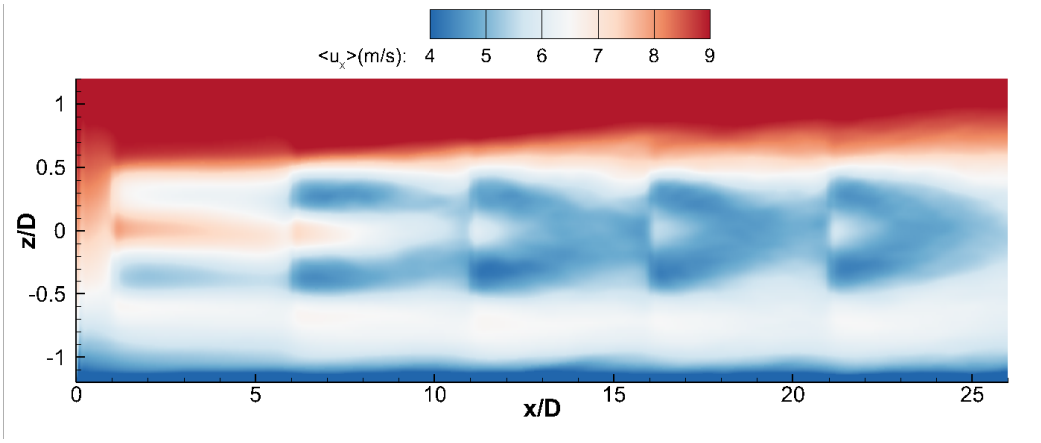

Figure 4.7. Mean velocity contour at y=0.

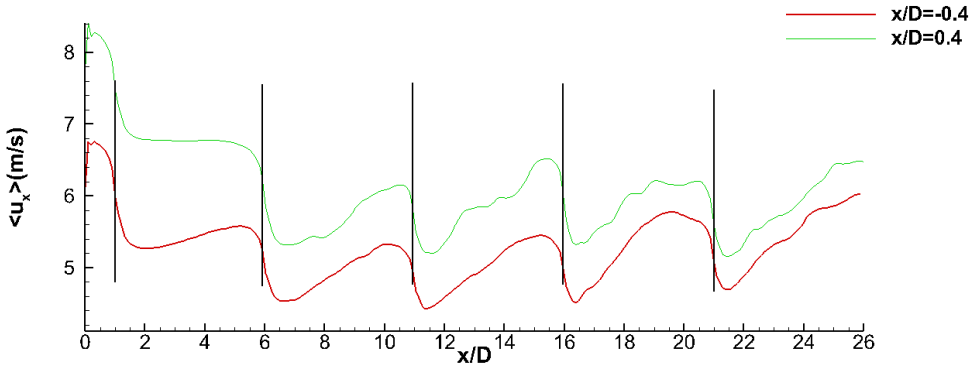

Figure 4.8. Mean velocity profile at the intersection of planes y=0 and z/D=-0.4 (lower one), the interaction of planes y=0 and z/D=0.4 (upper one).

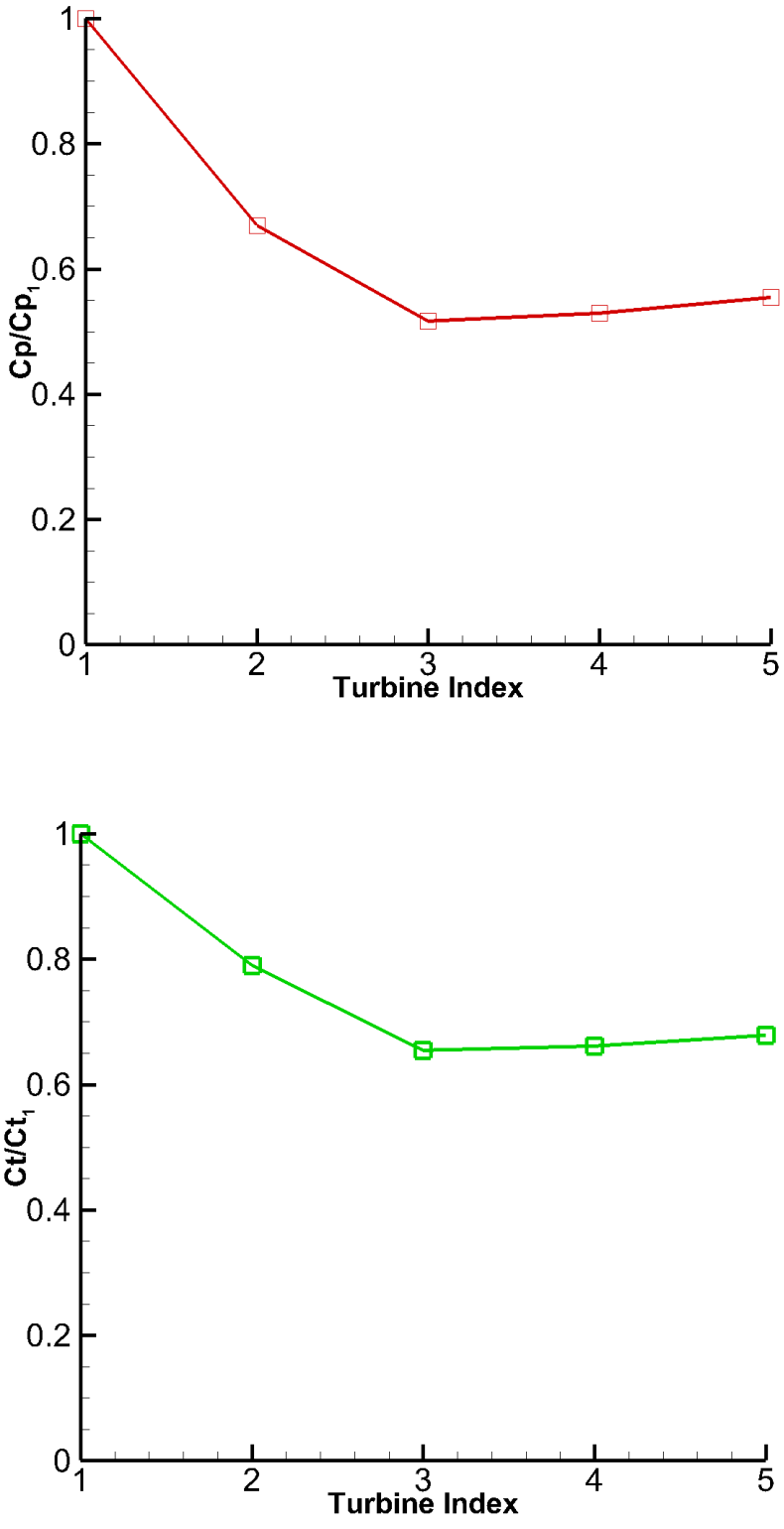

Figure 4.9. Power and thrust coefficients of five turbines.

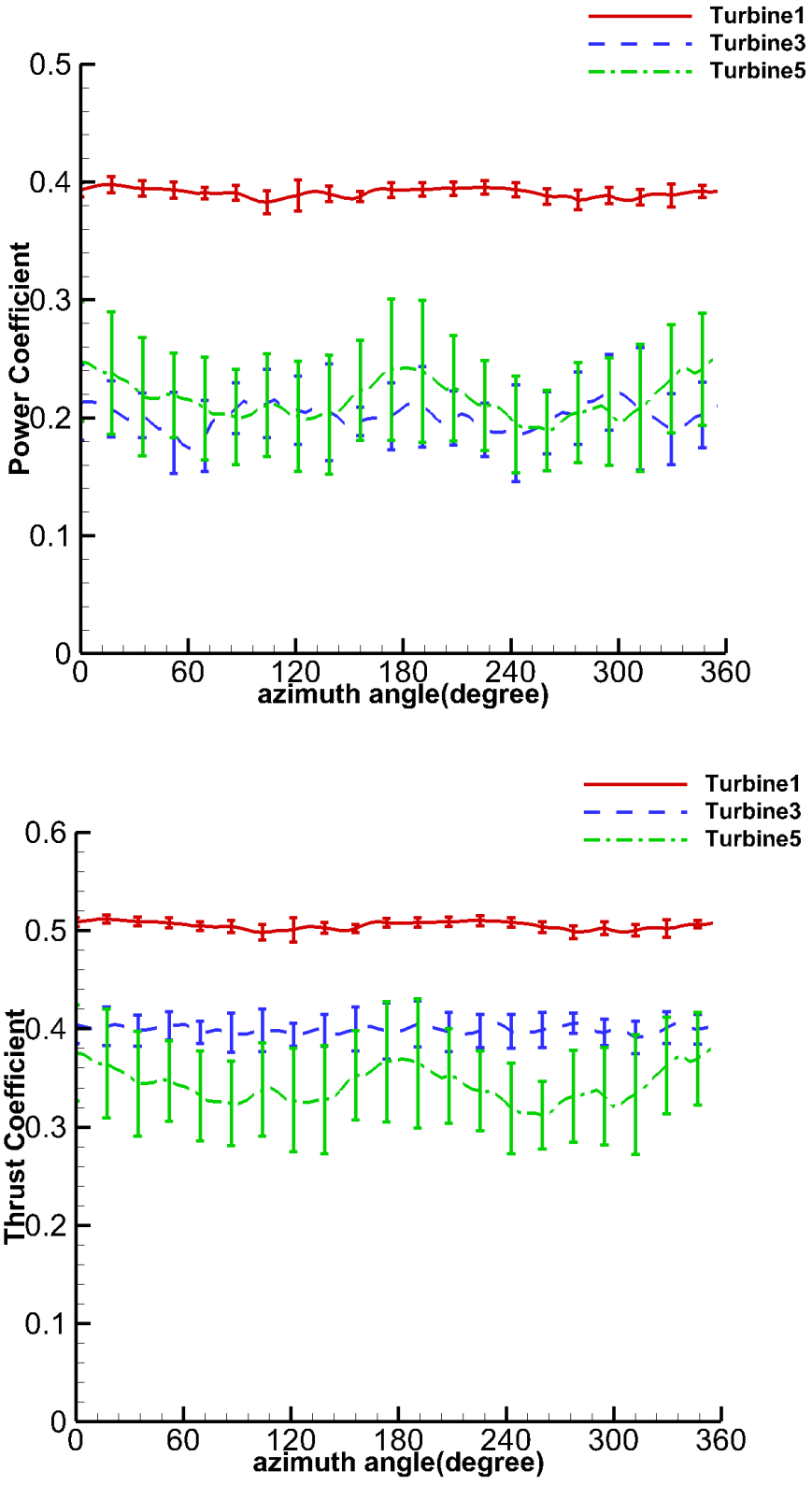

Figure 4.10. Comparison of phase averaged power and thrust coefficients. Error bars give the corresponding rms values.

at plane $z = 0$. The magnitude of the vertical velocity in the wake demonstrates the rotation of the wake. We can see after the second row, the wake rotation becomes weaker and weaker. This is brought by the turbulence induced wake recovery. Faster wake recovery means stronger turbulence. Each turbine is a source for turbulence, so the wake becomes more turbulent at further downstream. Figure 4.12 shows the isosurface of $U_{inlet} - < u_x >= 1$ m/s. In this figure, one can observe that all the downstream turbines work in the wakes of upstream turbines. In this case, the wakes of upstream turbines will have a very big impact on the power outputs and loadings on the downstream turbines.

Tables 4.2 and 4.3 show the distribution of normalized power coefficients and thrust coefficients in the full wake setting (0^o inflow angle). In both tables, we can observe the same trend for all the five columns. The values of the coefficients decrease from the first row to the third row, but increase from the third row to the fifth row. The power and thrust coefficients of the five columns are similar, especially in the first row (from T_{11} to T_{51}), but in other rows, power and thrust coefficients display certain level of difference. This difference is brought by the interactions between turbines, not only in streamwise direction, but also in lateral direction. Although the interactions between turbines in lateral direction affect the symmetry of the "Cp-matrix" and the "Ct-matrix" as shown in tables 4.2 4.3, the symmetry of the full wake setting still dominates. For total Cp, the third column is the largest, but it is only 1.33 % larger than the first column, which is smallest in total Cp. The same trend also happens for total Ct: the largest total Ct is observed in the third column, which is only 1.13 %

Table 4.2. Normalized power coefficients (Cp_{ij}/Cp_{11}) distribution in full wake setting.

j/i	1	2	3	4	5
1	1.00	1.00	1.00	1.00	1.00
2	0.61	0.61	0.62	0.61	0.62
3	0.41	0.40	0.43	0.41	0.40
4	0.46	0.45	0.47	0.48	0.47
5	0.52	0.54	0.52	0.52	0.52
subtotal	3.00	3.00	3.04	3.02	3.01

Table 4.3. Normalized power coefficients (Ct_{ij}/Ct_{11}) distribution in full wake setting.

j/i	1	2	3	4	5
1	1.00	1.00	1.00	1.00	1.00
2	0.74	0.74	0.75	0.74	0.75
3	0.56	0.54	0.57	0.55	0.55
4	0.59	0.59	0.60	0.61	0.60
5	0.65	0.66	0.65	0.65	0.65
subtotal	3.54	3.53	3.57	3.55	3.55

larger than the second column, which is the smallest in total Ct. The distributions of power coefficients and thrust coefficients are also shown in figure 4.14, which indicates the same trend as we observed in tables 4.2 and 4.3.

Figure 4.15 compares velocity profiles at different downstream locations. The first profile is sampled from the inlet boundary $x = 0$. All other profiles are sampled at locations 1D after the rotor planes of T_{31}, T_{32}, T_{33}, T_{34} and T_{35}. One can observe velocity deficit after each turbine. The trends of velocity deficit here coincides with the trends shown in figure 4.8. The velocity deficit becomes more and more severe from T_{31} to T_{33}, but less severe from T_{33} to T_{35}, which explains the trends of Ct and Cp as the position goes downstream.

Figures 4.16 and 4.17 demonstrate the comparison of normalized turbulent kinetic energy (TKE) $k = \langle u'^2 + v'^2 + w'^2 \rangle$ and production term $\mathcal{P}$ at different downstream locations. The locations selected here are the same as the locations selected for figure 4.15. The transport equation of k for incompressible flow is:

$$\frac{\partial k}{\partial t} + \langle u_i \rangle \frac{\partial k}{\partial x_i} = \mathcal{P} - \varepsilon - \frac{\partial T_i'}{\partial x_i}, \tag{4.5}$$

where $\varepsilon = 2\nu \langle S_{ij} S_{ij} \rangle$ is the dissipation term, $\mathcal{P}$ is the production term, and $T_i' = \frac{1}{2}\langle u_i' u_j' u_j' \rangle + \langle u_i' p' \rangle / \rho - 2\nu \langle u_j' S_{ij} \rangle$ is the turbulence transport term. $\mathcal{P}$ represents the energy transfer from the mean flow to small scale turbulence.

TKE are calculated in the procedures below in this work. We all know that

$$U = \langle U \rangle + u' = \tilde{U} + u_{SGS}, \tag{4.6}$$

where $\langle U \rangle$ is the mean velocity, u' is velocity fluctuation, $\tilde{U}$ is the filtered velocity, and $u_{residual}$ is the residual velocity. If we assume $u_{residual}$ is negligible, then we can have

$$u' = \tilde{U} - \langle U \rangle, \tag{4.7}$$

where $\langle U \rangle$ is obtained with a time average of 1666 time steps (20 circles) as mentioned in 4.1, $\tilde{U}$ is solved from the filtered Navier-Stokes equations. Reynolds stress can be calculated via the outer product between u' and u'.

$$\mathcal{R} = u' \star u' = \begin{bmatrix} u_1 \\ u_2 \\ u_3 \end{bmatrix} \begin{bmatrix} u_1 u_2 u_3 \end{bmatrix} = \begin{bmatrix} \mathcal{R}_{11} & \mathcal{R}_{12} & \mathcal{R}_{13} \\ \mathcal{R}_{21} & \mathcal{R}_{22} & \mathcal{R}_{23} \\ \mathcal{R}_{31} & \mathcal{R}_{32} & \mathcal{R}_{33} \end{bmatrix}. \tag{4.8}$$

Then TKE k can be calculated with the trace of $\mathcal{R}$.

$$k = 0.5 trace(\mathcal{R}) = 0.5(\mathcal{R}_{11} + \mathcal{R}_{22} + \mathcal{R}_{33}). \tag{4.9}$$

Production $\mathcal{P}$ can be calculated with double inner product between mean strain rate $\mathcal{S}$ and mean Reynolds stress $\mathcal{R}$.

$$\mathcal{P} = -\langle \mathcal{S} \rangle : \langle \mathcal{R} \rangle \tag{4.10}$$

Here the mean strain rate and mean Reynolds strss are obtained by taking time-average for 20 revolutions (1666 time steps).

In figure 4.16, one can observe that the normalized TKE increases from T_{31} to T_{35}, but the increase between every two adjacent turbines are different. TKE behind the first turbine T_{31} is quite small. Its maximum value is about 0.004 at the top tip $z/D = 0.5$, which increases downstream. The normalized TKE does not change

so much from $x/D = 0$ to $x/D = 7$ and from $x/D = 12$ to $x/D = 22$, but the difference between $x/D = 7$ and $x/D = 12$ is very big. This means turbulence has a steep increase. From $x/D = 7$ to $x/D = 12$, the maximum value for normalized TKE increases from about 0.008 at $z/D = 0.5$ to 0.028 at around $z/D = 0.5$. In this distance, another peak at the bottom tip $z/D = -0.5$ appears. It increases from 0.002 to 0.006. Behind $x/D = 12$, the third peak of normalized TKE appears near the ground, and it keeps increasing. This is because of the sudden drop of the more unsteady velocity near the ground. The peak values at the top tip is larger than the peak values at the bottom tip, which is the same as observed in [12, 29]. The peak value at the bottom tip increases a little bit from $x/D = 12$ to $x/D = 22$, but the peak value at the top tip nearly remains constant. The average normalized TKE in the blade swept area increases a little bit from $x/D = 12$ to $x/D = 22$. This trend is like the trend in figure 4.15. Immediately behind the third turbine, TKE becomes much larger than upstream, wake recovery becomes more obvious, and the power coefficients and thrust coefficients stop from decreasing behind the third turbine. The sudden increase of TKE immediately behind the third turbine should be responsible for this.

In figure 4.17, one can observe the similar trend as TKE. The profiles for $\mathcal{P}$ have three peaks at different downstream locations. The first one is at the top tip ($z/D = 0.5$). The second one appears at the bottom tip ($z/D = -0.5$). The third one is near the ground. At $x/D = 2$ the maximum magnitude of $\mathcal{P}$ is around 0.06. From T_{31} to T_{33}, there are big growths in both the peaks at the top tip and the bottom tip.

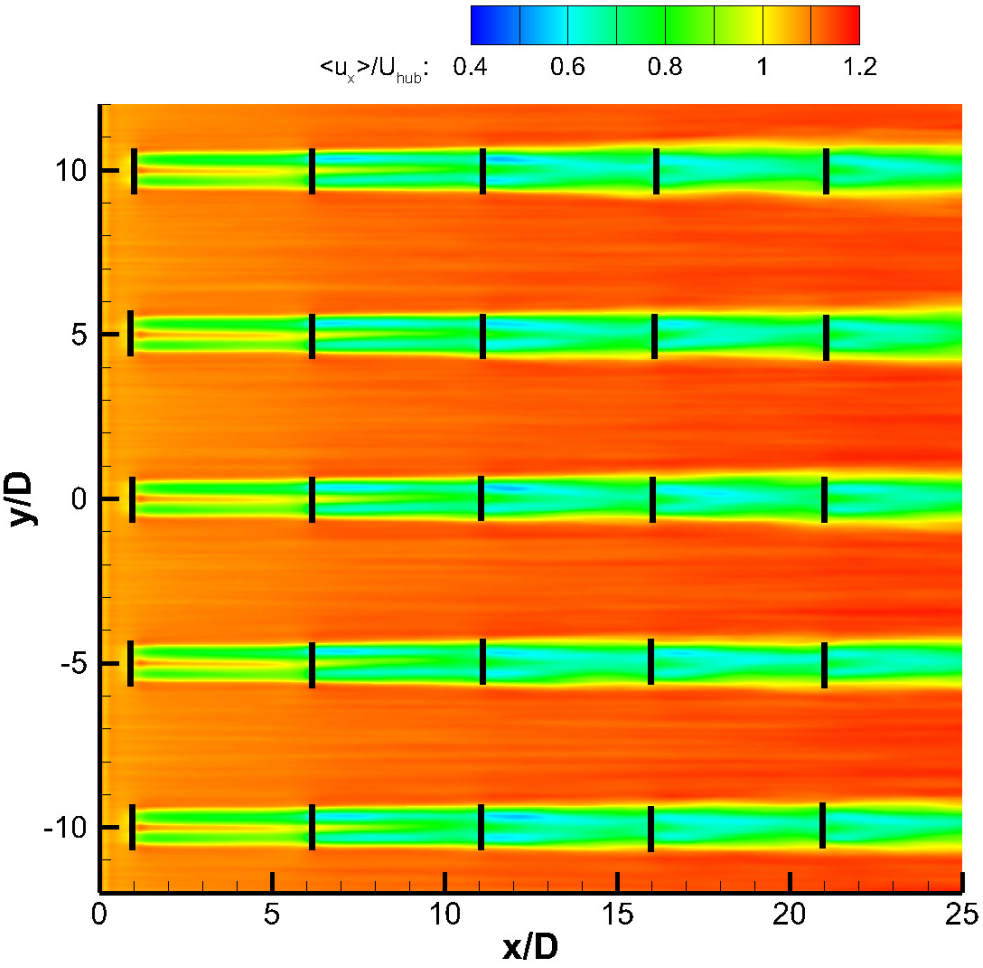

Figure 4.11. Normalized streamwise mean velocity at plane $z = 0$ in the full wake setting (zero inflow angle).

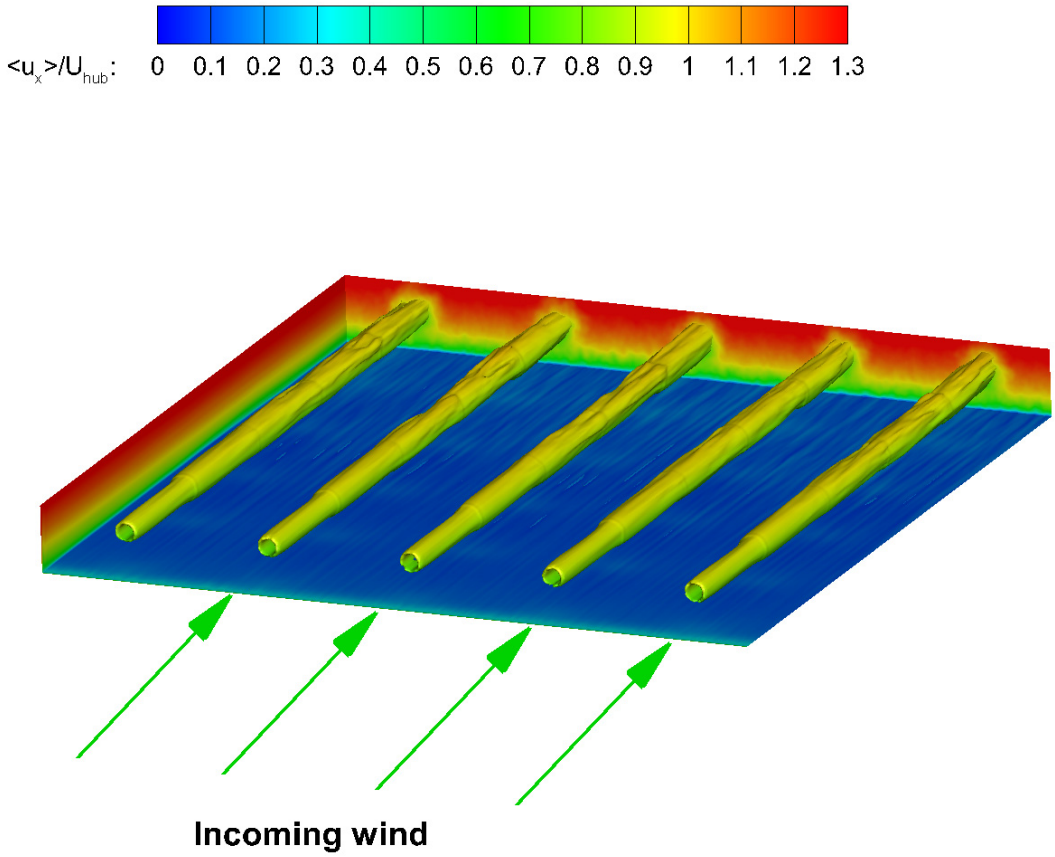

Figure 4.12. Isosurface of $U_{inlet} - < u_x >= 1$ m/s in the full wake setting (zero inflow angle).

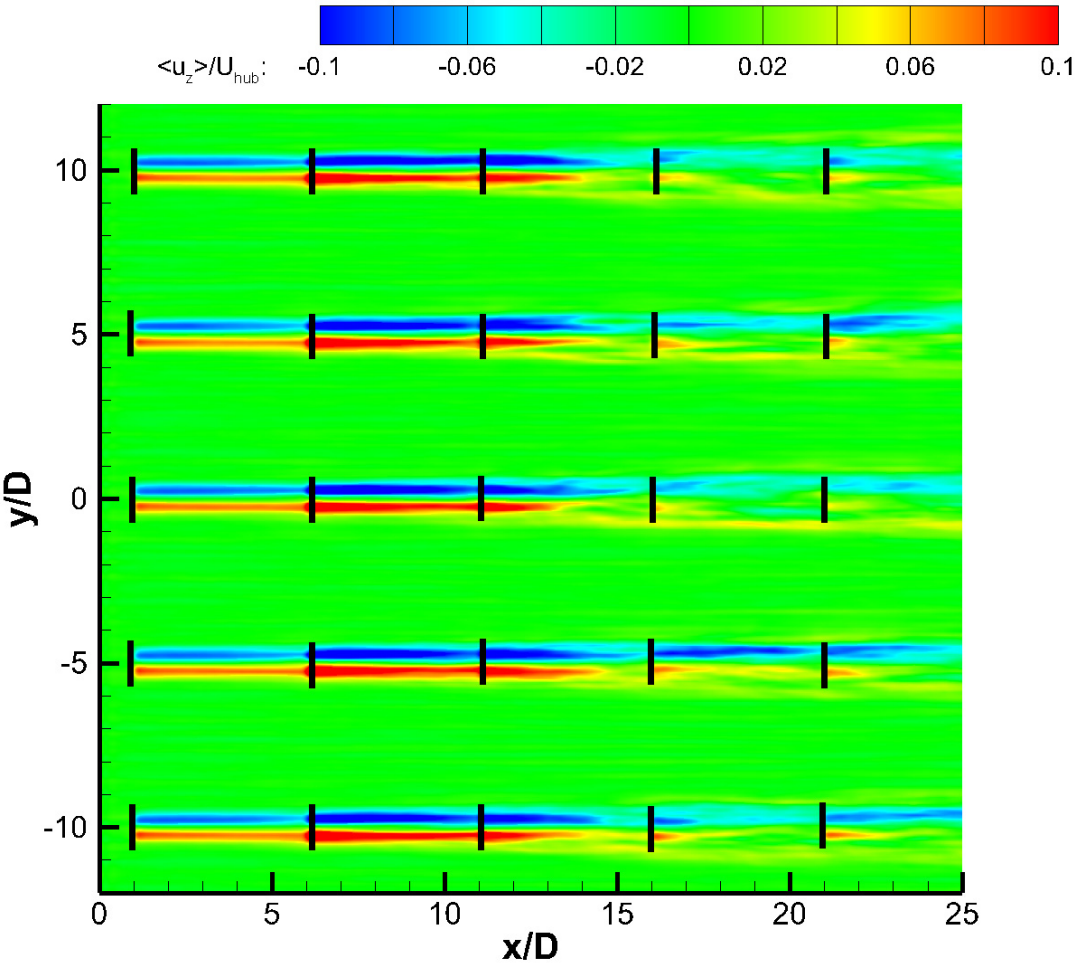

Figure 4.13. Normalized vertical mean velocity at plane $z = 0$ in the full wake setting (zero inflow angle).

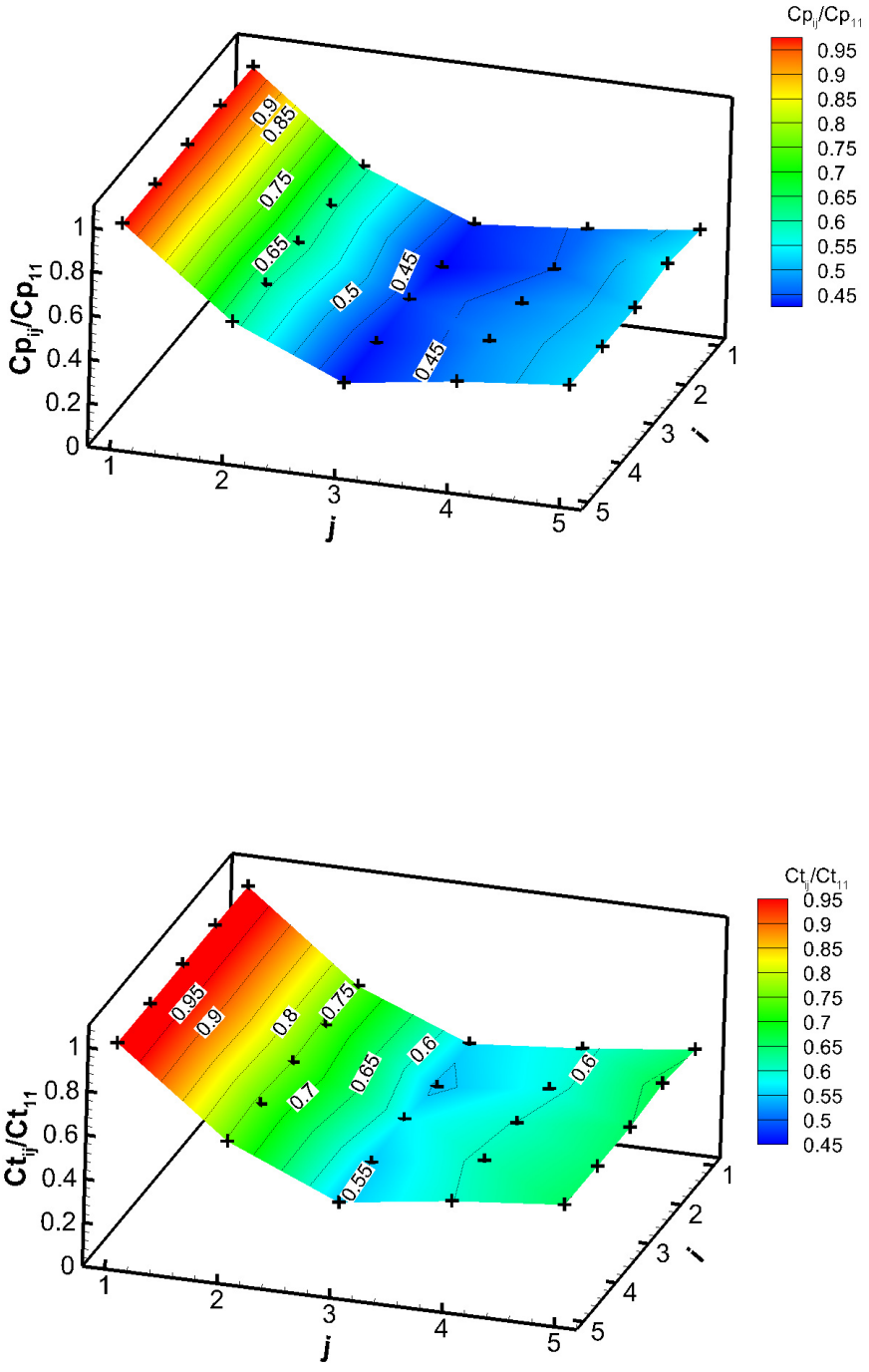

Figure 4.14. Distribution of normalized Cp and Ct in full wake setting.

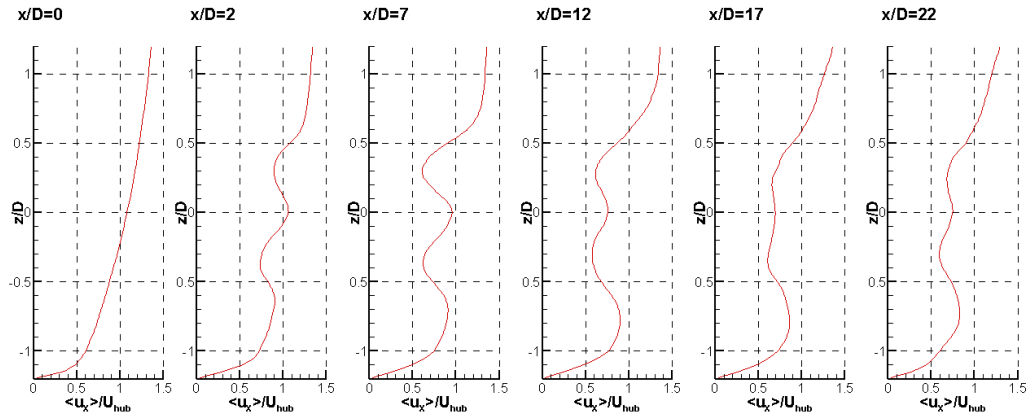

Figure 4.15. Comparison of mean streamwise velocity at different downstream locations.

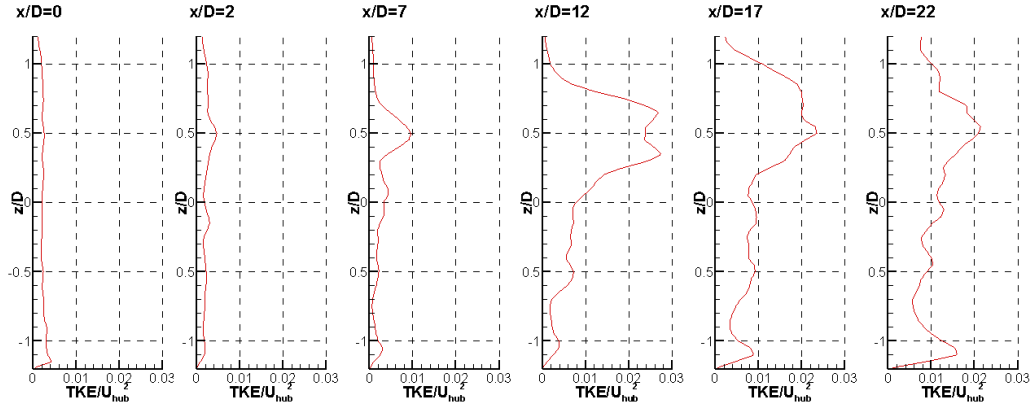

Figure 4.16. Comparison of TKE at different downstream locations.

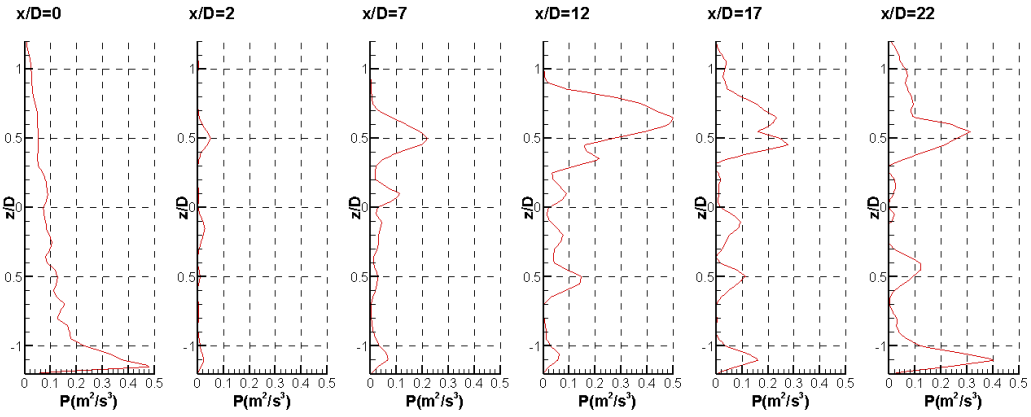

Figure 4.17. Comparison of $\mathcal{P}$ at different downstream locations.

For the top tip, the peak value increases from 0.06 to 0.48. For the bottom tip, the peak value increases from 0.02 to 0.14. There is also a relatively moderate increase for the peak near the ground. On the contrary, from T_{33} to T_{35}, the peak values at both top and bottom tips decrease, while the peak value near the ground keeps increasing. For the top tip, $\mathcal{P}$ decreases from 0.48 to around 0.3. For the bottom tip, $\mathcal{P}$ decreases from 0.14 to around 0.12. Based on the above discussion, the average $\mathcal{P}$ in the blade swept area increases from T_{31} to T_{33}, but decreases from T_{33o} to T_{35}. $\mathcal{P}$ is calculated via the double inner product between mean strain rate $\mathcal{S}$ and mean Reynolds stress $\mathcal{R}$. Strain rate is the symmetric part of velocity gradient. The mean velocity gradient is the largest at planes $z/D = 0.5$ and $z/D = -0.5$, which leads to large strain rate, which further results in large $\mathcal{P}$. Because TKE at $z/D = 0.5$ is much larger than the TKE at $z/D = -0.5$, $\mathcal{P}$ at $z/D = 0.5$ is still larger than the production at $z/D = -0.5$.

Figure 4.18 shows the normalized mean streamwise velocity of 15^o inflow angle at plane $z = 0$. Figure 4.19 shows the isosurface of $U_{inlet} - < u_x >= 1$ m/s. In this figure, one can observe that the downstream turbines in this case do not work in the wakes of upstream turbines, so the impacts of upstream turbines on the Cp and Ct of downstream turbines are not big. Tables 4.4 and 4.5 show the distribution of normalized power coefficients and thrust coefficients under 15^o inflow angle. In both tables, we can see that for the first row, second row, third row and fourth row in table 4.4, Cp and Ct are larger than or equal to one. This is because of the direct exposure of the whole turbine rotors or most of the turbine rotors to the incoming

flow from the inlet boundary. This is also because of the effects from the turbines in lateral directions. Let's take T_{22} as an example. In its rotor plane, there are several low speed areas introduced by the wakes of T_{21}, T_{11}, T_{12}, T_{13}, T_{14} and T_{15}. Because this is not an infinite wide domain, these low speed areas make the incoming speed for the turbines whose Cp is larger than one higher than T_{11}. This is why they have Cp larger than one. To clarify this incoming speed difference, T_{11} and T_{33} are picked for comparison. In figure 4.20, $x/D = 0.5$ represents the plane 0.5D in front of the rotor plane of T_{11}, and $x/D = 12.7$ is the plane 0.5D in front of T_{33}. The rotor of T_{11} is bounded by $y/D = -0.5$ and $y/D = 0.5$, $z/D = -0.5$ and $z/D = 0.5$. The rotor of T_{33} is bounded by $y/D = 6.5$ and $y/D = 7.5$, $z/D = -0.5$ and $z/D = 0.5$. One can clearly identify that the incoming speed for T_{33} is higher than that of T_{11}. This incoming speed difference makes the Cp difference mentioned above, and this incoming speed difference is brought by the wakes of upstream turbines in lateral direction. For other turbines (the fifth row), Cp and Ct are smaller than one, but still larger than 0.9, because these turbines work in partial wake. If one compares this partial wake setting case with the full wake setting case, it can be found out that the total power output of the active wind farm increases dramatically from full wake setting to partial wake setting, so the partial wake working condition may enhance the power output, but increase the aerodynamic loadings of the active wind farm. The distributions of power coefficients and thrust coefficients are also shown in figure 4.21.

Table 4.4. Normalized power coefficients (Cp_{ij}/Cp_{11}) distribution under 15^o inflow angle.

j/i	1	2	3	4	5
1	1.00	1.00	1.00	1.01	1.01
2	1.01	1.03	1.03	1.04	1.04
3	1.02	1.05	1.06	1.06	1.07
4	1.02	1.08	1.06	1.09	1.05
5	1.04	0.99	0.94	0.97	0.96
subtotal	5.22	5.15	5.09	5.17	5.13

Table 4.5. Normalized power coefficients (Ct_{ij}/Ct_{11}) distribution under 15^o inflow angle.

j/i	1	2	3	4	5
1	1.00	1.00	1.00	1.01	1.01
2	1.01	1.02	1.02	1.02	1.02
3	1.02	1.03	1.03	1.03	1.04
4	1.04	1.04	1.03	1.05	1.02
5	1.05	1.00	0.97	0.98	0.98
subtotal	5.07	4.87	4.90	4.95	4.95

Table 4.6. Normalized power coefficients (Cp_{ij}/Cp_{11}) distribution under 30^o inflow angle.

j/i	1	2	3	4	5
1	1.00	1.00	1.00	1.01	1.03
2	1.01	1.03	1.03	1.05	1.04
3	1.02	0.93	0.95	0.96	0.95
4	1.04	0.93	0.95	0.98	0.98
5	1.06	0.95	0.96	0.95	0.96
subtotal	5.13	4.84	4.89	4.95	4.96

Figure 4.22 shows the normalized mean streamwise velocity of 30^o inflow angle at plane $z = 0$. Figure 4.23 shows the isosurface of $U_{inlet} - < u_x >= 1$ m/s. In this figure, one can observe that the downstream turbines are slightly impacted by the wakes of upstream turbines. Tables 4.6 and 4.7 show the distribution of normalized power coefficients and thrust coefficients under 30^o inflow angle. One can see that for the first column, first row and second row in figure 4.6, the values for normalized Cp and Ct are larger than or equal to one for the same reason discussed for 15^o inflow angle. For other turbines, Cp and Ct are between 1 and 0.9. As discussed for the wind farm under 15^o inflow angle, the partial wake working condition may enhance the power output of the active wind farm. This can be validated again by the comparison of total Cp between full wake case and 30^o angle case. The distributions of power coefficients and thrust coefficients are also shown in figure 4.14, which indicates the same trend as we observed in tables 4.6 and 4.7.

Tables 4.8 and 4.9 show the distribution of normalized Cp and Ct under 45^o inflow angle. Figure 4.25 shows the time averaged normalized streamwise direction at $z = 0$ plane. Figure 4.26 shows the isosurface of $U_{inlet} - < u_x >= 1$ m/s. One can observe

Table 4.7. Normalized power coefficients (Ct_{ij}/Ct_{11}) distribution under 30^o inflow angle.

j/i	1	2	3	4	5
1	1.00	1.00	1.00	1.01	1.02
2	1.01	1.01	1.02	1.03	1.02
3	1.01	0.95	0.96	0.97	0.96
4	1.02	0.95	0.96	0.98	0.98
5	1.03	0.96	0.96	0.96	0.97
subtotal	5.07	4.87	4.90	4.95	4.95

Table 4.8. Normalized power coefficients (Cp_{ij}/Cp_{11}) distribution under 45^o inflow angle.

j/i	1	2	3	4	5
1	1.00	1.00	1.02	1.02	1.05
2	1.01	0.63	0.61	0.62	0.66
3	1.02	0.60	0.51	0.53	0.54
4	1.02	0.61	0.54	0.63	0.60
5	1.04	0.63	0.59	0.62	0.61
subtotal	5.09	3.47	3.27	3.42	3.46

Table 4.9. Normalized power coefficients (Ct_{ij}/Ct_{11}) distribution under 45^o inflow angle.

j/i	1	2	3	4	5
1	1.00	0.99	1.00	1.01	1.02
2	0.99	0.74	0.73	0.74	0.77
3	1.00	0.72	0.64	0.65	0.66
4	1.00	0.73	0.66	0.73	0.71
5	1.01	0.74	0.70	0.72	0.71
subtotal	5.00	3.92	3.73	3.85	3.87

that more than half of the turbines work in full wake, so this inflow angle is not good for power output. In the two tables, we can see that for the first column and first row in table 4.8, the values for normalized Cp and Ct are larger than or equal to one for the same reason discussed for 15^o inflow angle. For other turbines, the values for normalized Cp and Ct are much smaller than one. It is similar to the case for wind farm under 0^o inflow angle, where the full wake setting decreases the power output of downstream turbines. The trends in figure 4.27 for the distributions of power coefficients and thrust coefficients are the same as what are observed in tables 4.8 and 4.9. From the comparison of all the for inflow angles, it can be concluded that wind farm under inflow angle near 15^o should be the best for power output.

From the results provided above, we can see that there is a significant increase in power output of the active wind farm from full wake setting to 15^o inflow angle. To better understand the change, we simulate the wind farm under a 5^o inflow angle. Figure 4.28 shows the normalized mean streamwise velocity at plane $z = 0$. Figure 4.29 shows the isosurface of $U_{inlet} - < u_x >= 1$ m/s. In this figure, one can observe that the downstream turbines are slightly impacted by the wakes of upstream turbines. Tables 4.10 and 4.11 shows the distribution of normalized power coefficients and thrust coefficients under 5^o inflow angle. Only the first row is exposed to the incoming wind from the inlet boundary, but all other turbines are in partial wake setting, which makes the power coefficients and thrust coefficients of the 5^o inflow angle case larger than the full wake setting case, but smaller than the 15^o inflow angle case. In the 5^o inflow angle case, the power and thrust coefficients decrease from the first row to the third row, but increase from the third row to the fifth row. This is like the full wake setting case. The partial wake setting makes the wind farm generate more power, which is like the 15^o inflow angle case. The distributions of power coefficients and thrust coefficients are also shown in figure 4.30.

We have tested the wind farm under five different inflow angles. Figure 4.31 shows the normalized power output of the active wind farm under different inflow angles. We can see that inflow angle and partial wake setting bring a great increase in power output. The power output increases from full wake setting to the 15^o inflow angle case, and decreases slightly from 15^o inflow angle case to the 45^o inflow angle case, so inflow angle near 15^o is close to the best arrangement for power output in wind farms.

Table 4.10. Normalized power coefficients (Cp_{ij}/Cp_{11}) distribution under 5^o inflow angle.

j/i	1	2	3	4	5
1	1.00	1.00	1.00	1.00	1.00
2	0.86	0.86	0.85	0.85	0.86
3	0.79	0.79	0.78	0.78	0.79
4	0.79	0.80	0.81	0.80	0.81
5	0.84	0.82	0.84	0.84	0.83
subtotal	4.28	4.27	4.28	4.27	4.29

Table 4.11. Normalized power coefficients (Ct_{ij}/Ct_{11}) distribution under 5^o inflow angle.

j/i	1	2	3	4	5
1	1.00	1.00	1.00	1.00	1.00
2	0.91	0.91	0.90	0.90	0.91
3	0.84	0.84	0.84	0.84	0.85
4	0.84	0.85	0.86	0.85	0.86
5	0.88	0.87	0.89	0.88	0.87
subtotal	4.47	4.47	4.49	4.47	4.47

Under 15^o inflow angle, there are only five turbines out of 25 working in partial wake or full wake condition, which is less than other partial wake settings 5^o inflow angle and 30^o inflow angle. For 0^o inflow angle and 45^o inflow angle, most of the turbines work in full wake setting, so the power outputs are surely lower than 15^o inflow angle. This is why 15^o inflow angle is near to the best arrangement for power output.

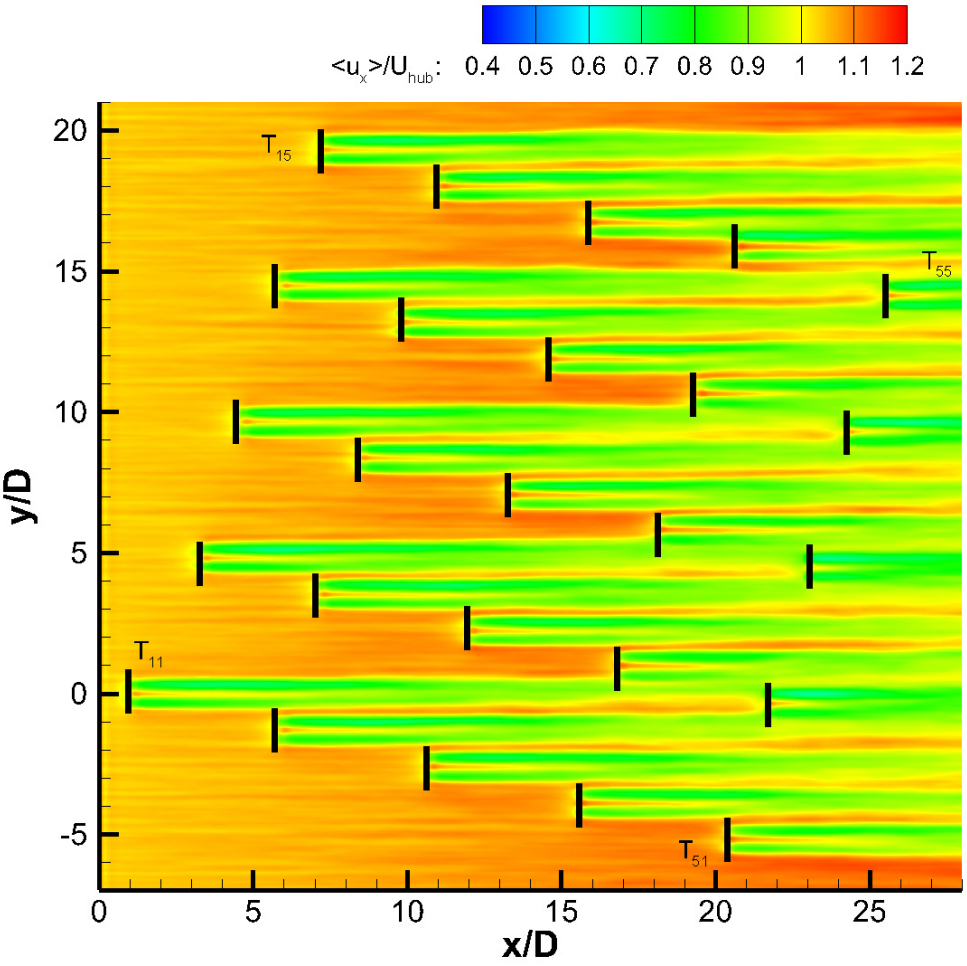

Figure 4.18. Normalized streamwise mean velocity at plane $z = 0$ under 15^o inflow angle.

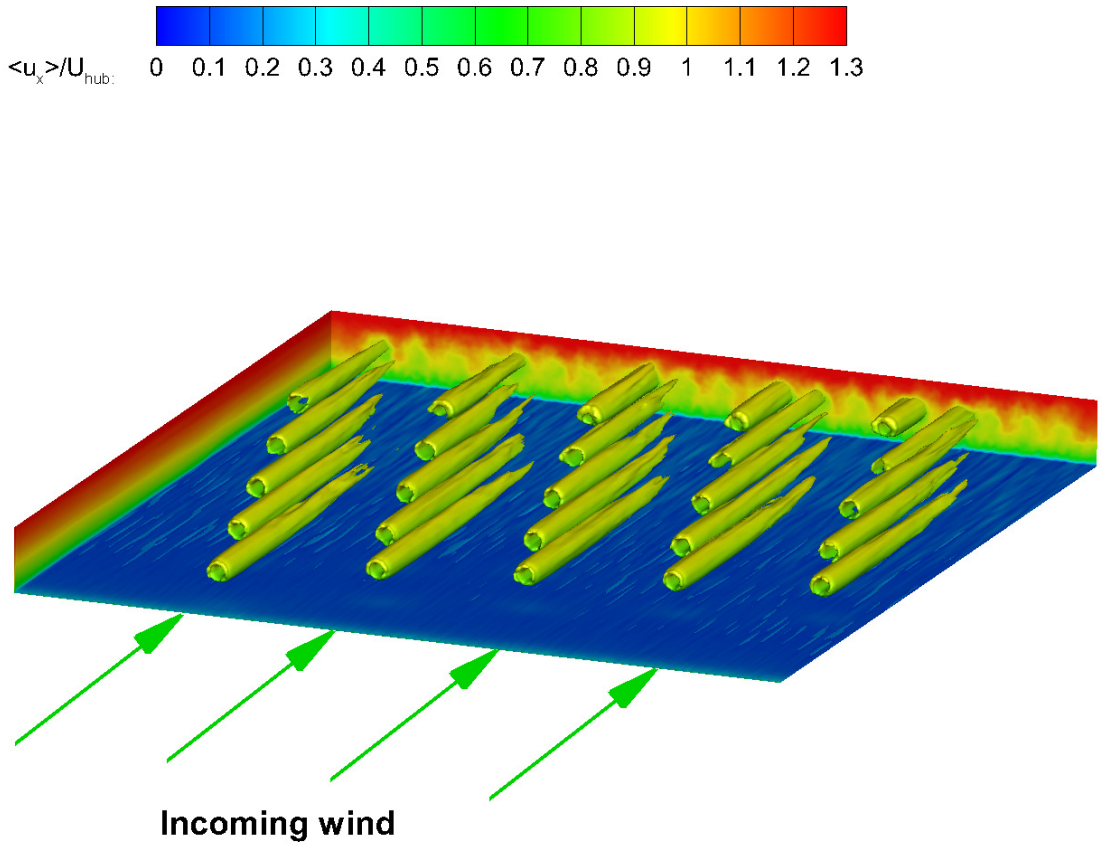

Figure 4.19. Isosurface of $U_{inlet} - < u_x >= 1$ m/s under 15^o inflow angle.

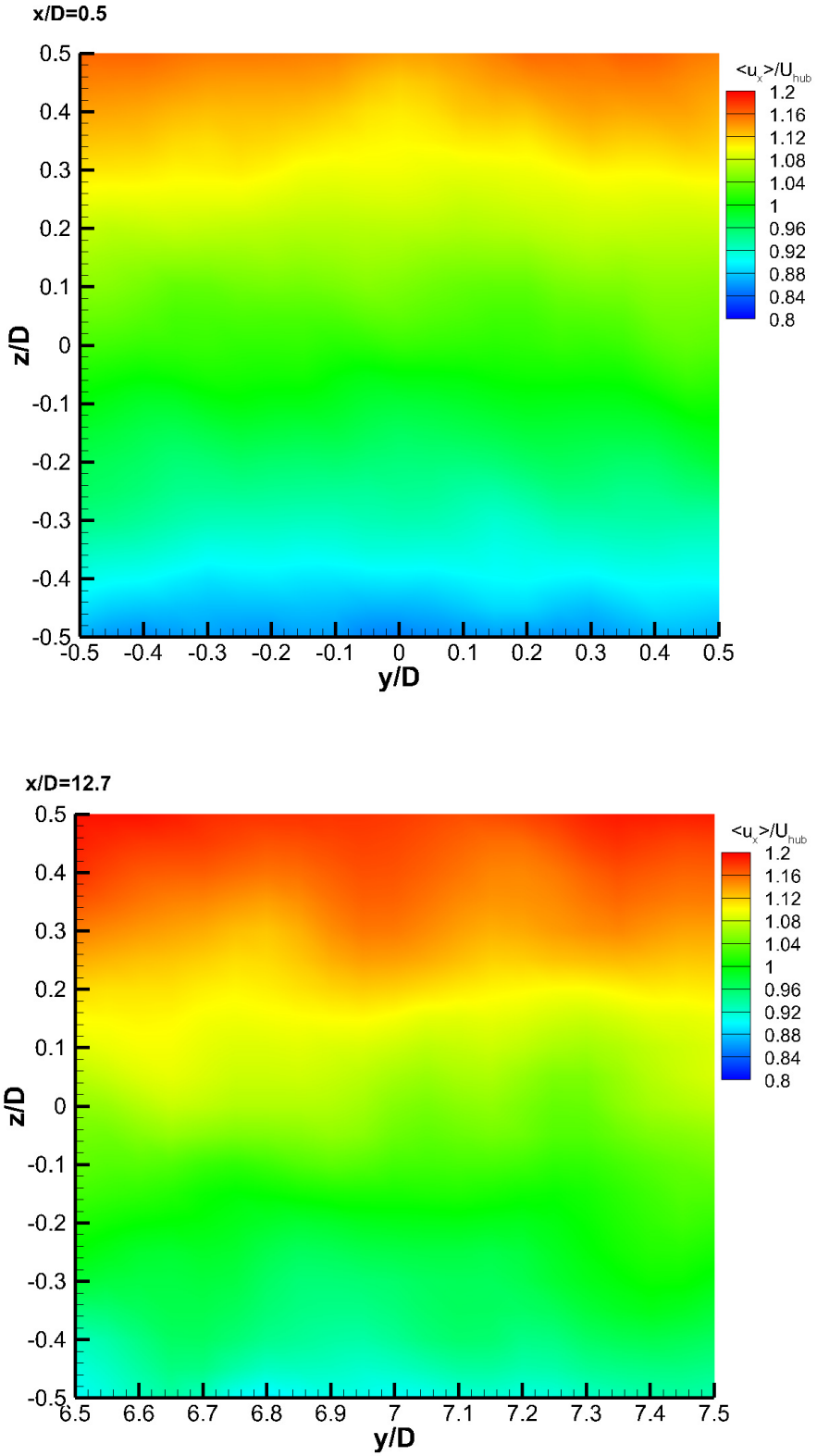

Figure 4.20. Comparison between velocity contours in the planes 0.5D infront of rotor planes of T_{11} and T_{33}.

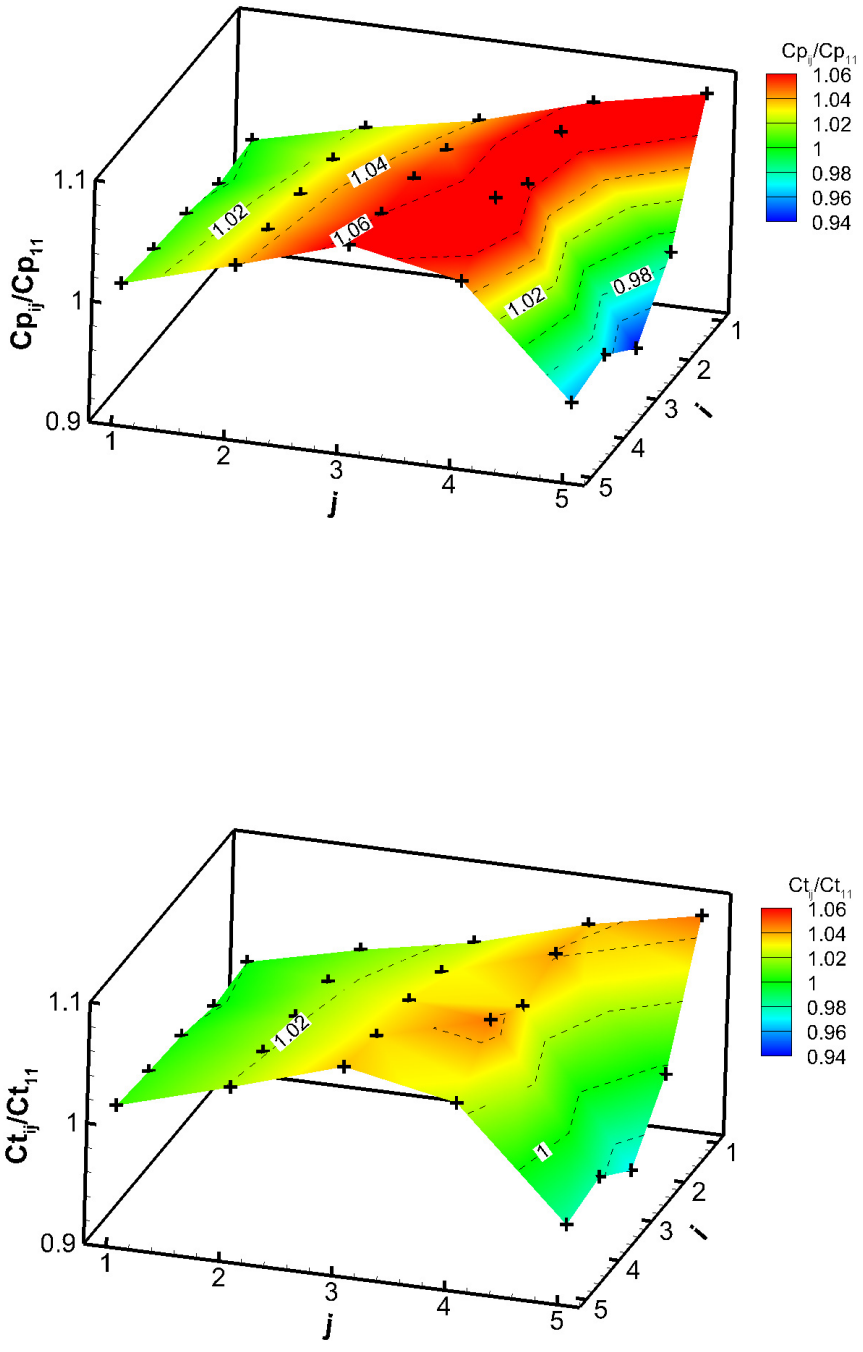

Figure 4.21. Distribution of normalized Cp and Ct under 15^o inflow angle.

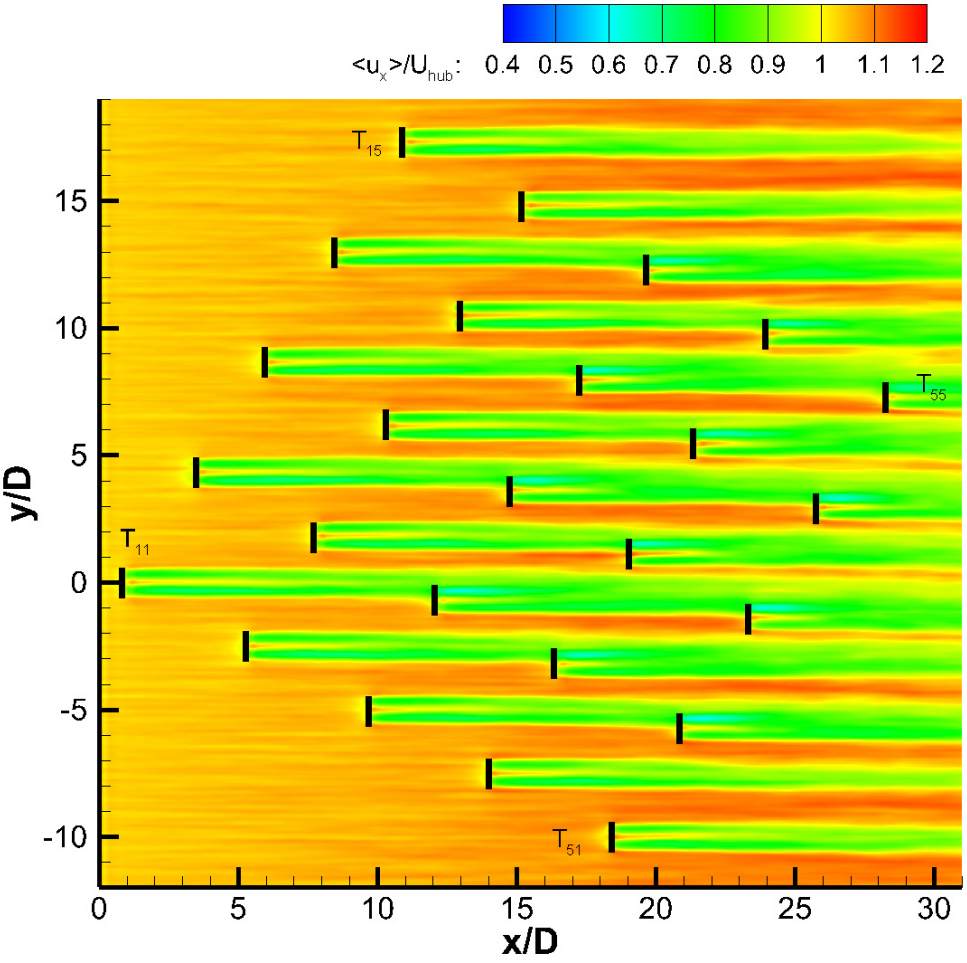

Figure 4.22. Normalized streamwise mean velocity at plane $z = 0$ under 30^o inflow angle.

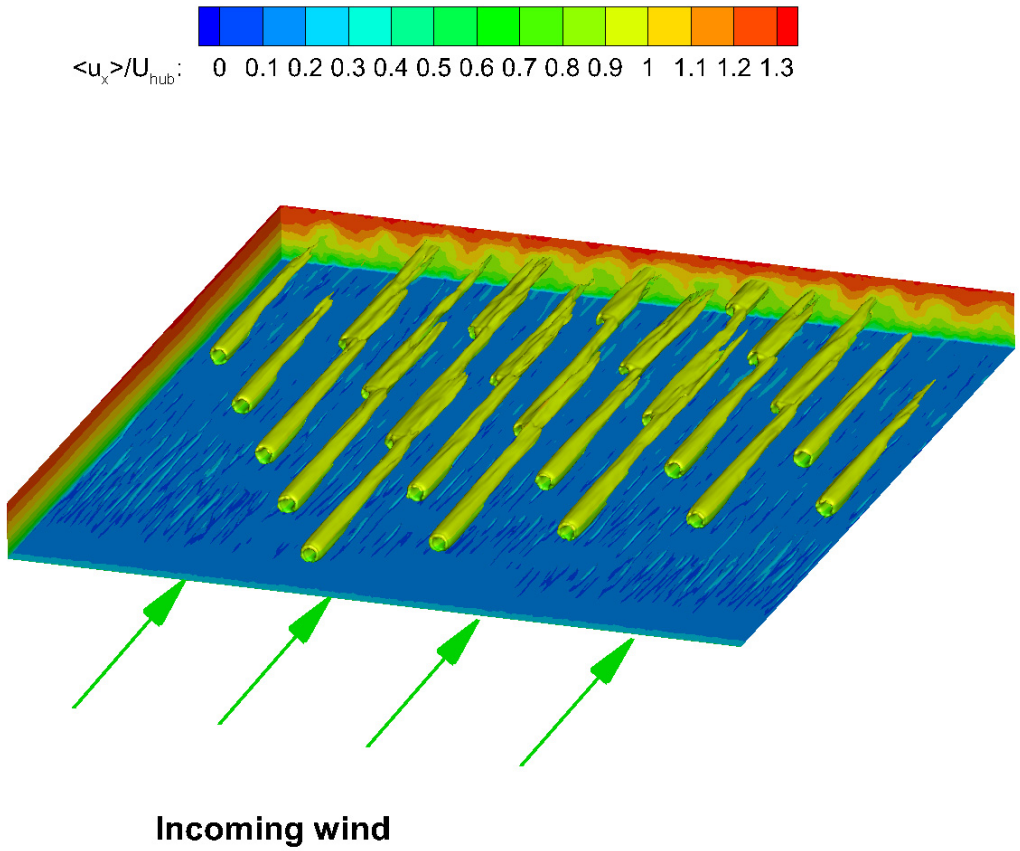

Figure 4.23. Isosurface of $U_{inlet} - < u_x >= 1$ m/s under 30^o inflow angle.

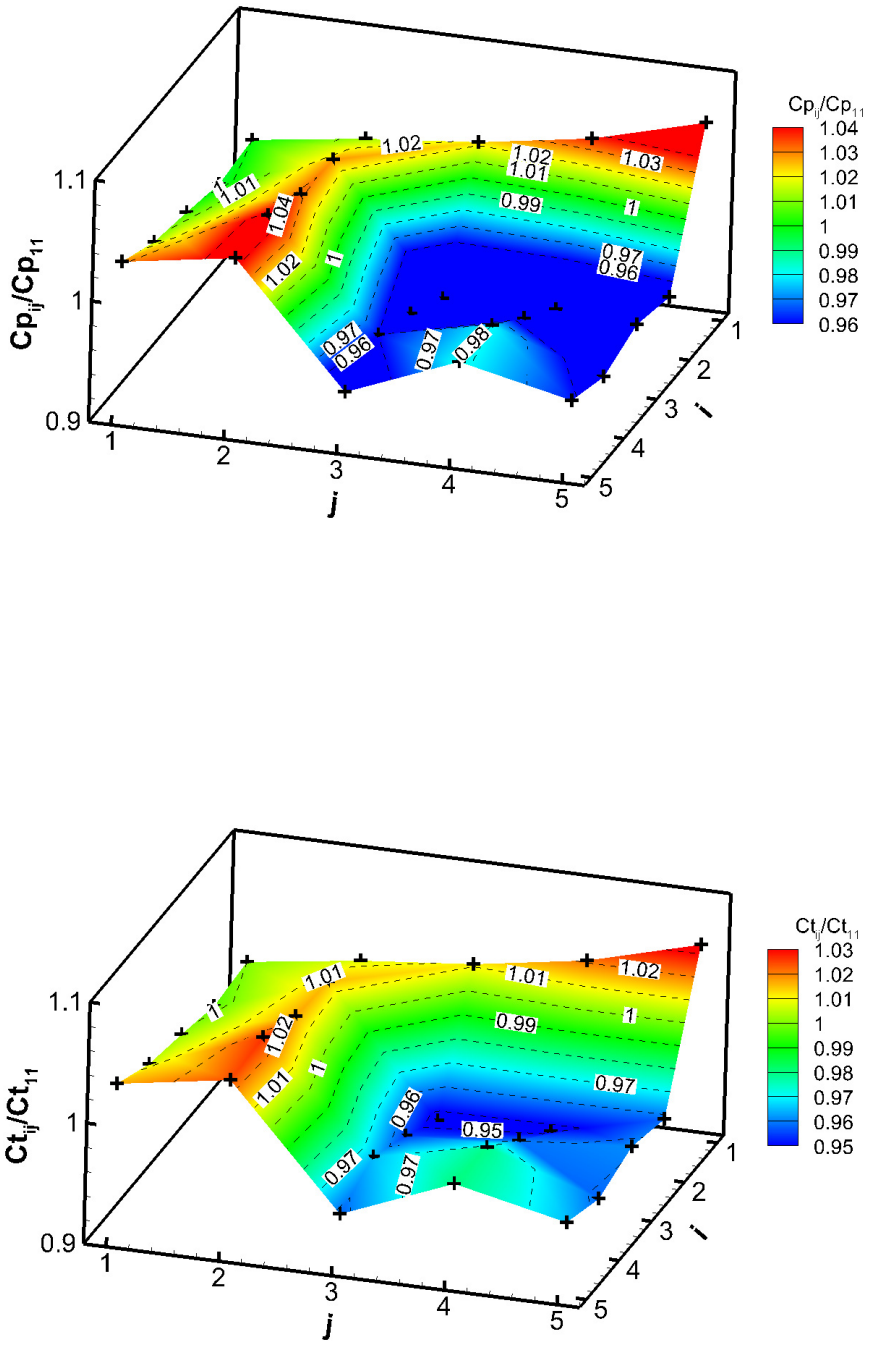

Figure 4.24. Distribution of normalized Cp and Ct under 30^o inflow angle.

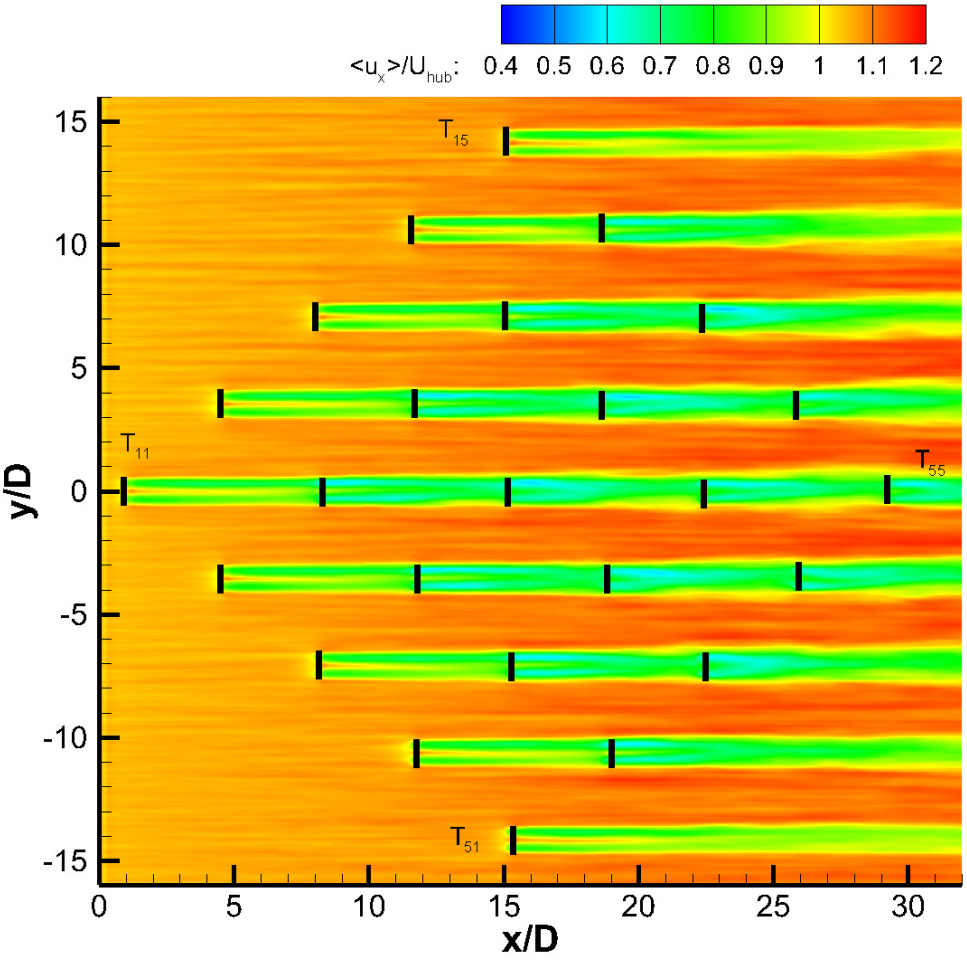

Figure 4.25. Normalized streamwise mean velocity at plane $z = 0$ under 45^o inflow angle.

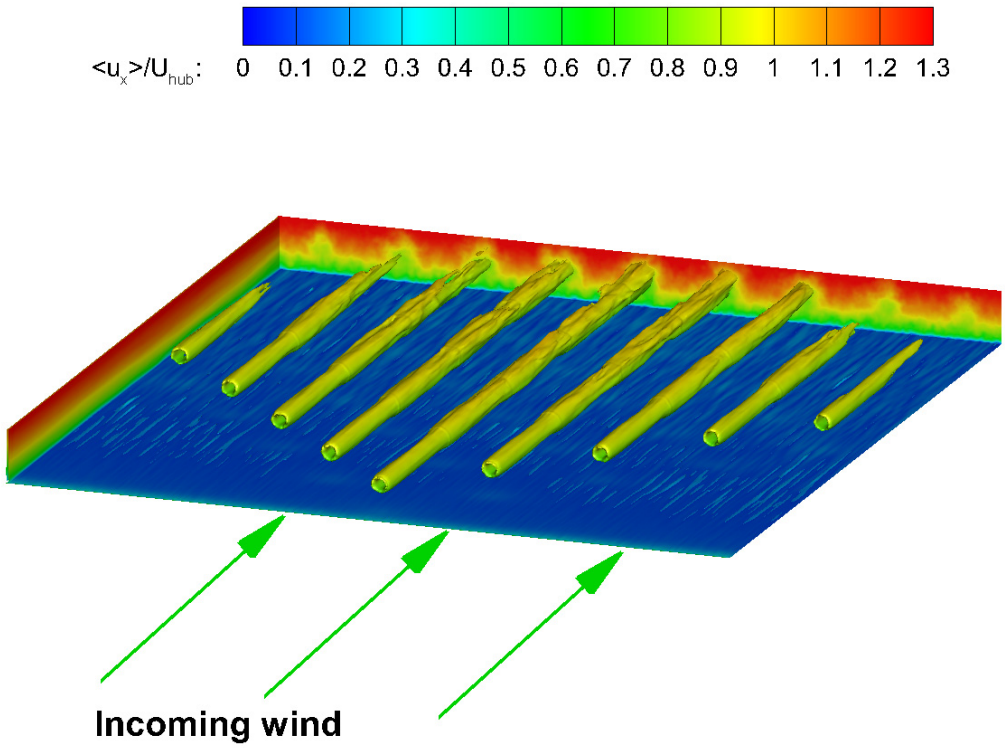

Figure 4.26. Isosurface of $U_{inlet} - < u_x >= 1$ m/s under 45^o inflow angle.

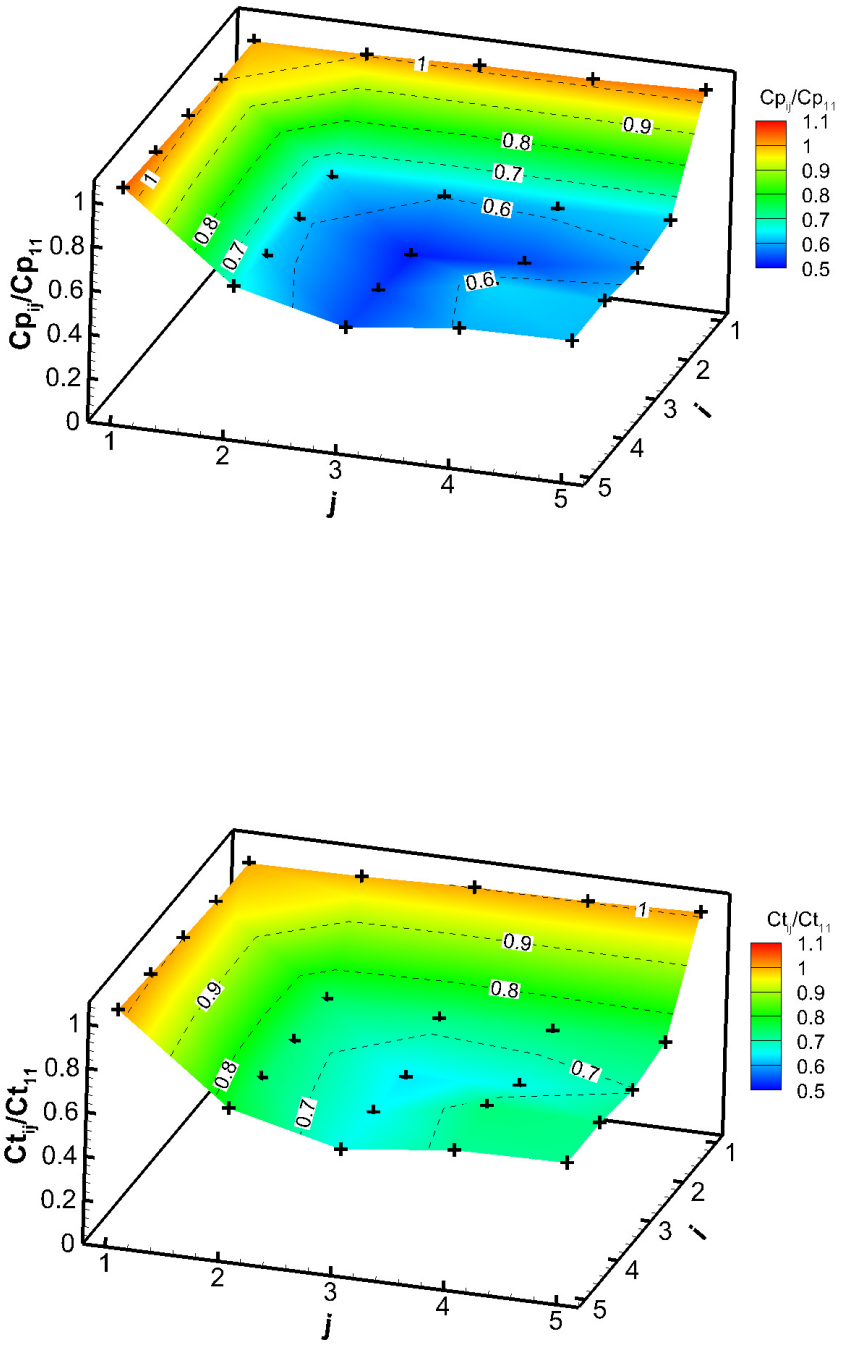

Figure 4.27. Distribution of normalized Cp and Ct under 45^o inflow angle.

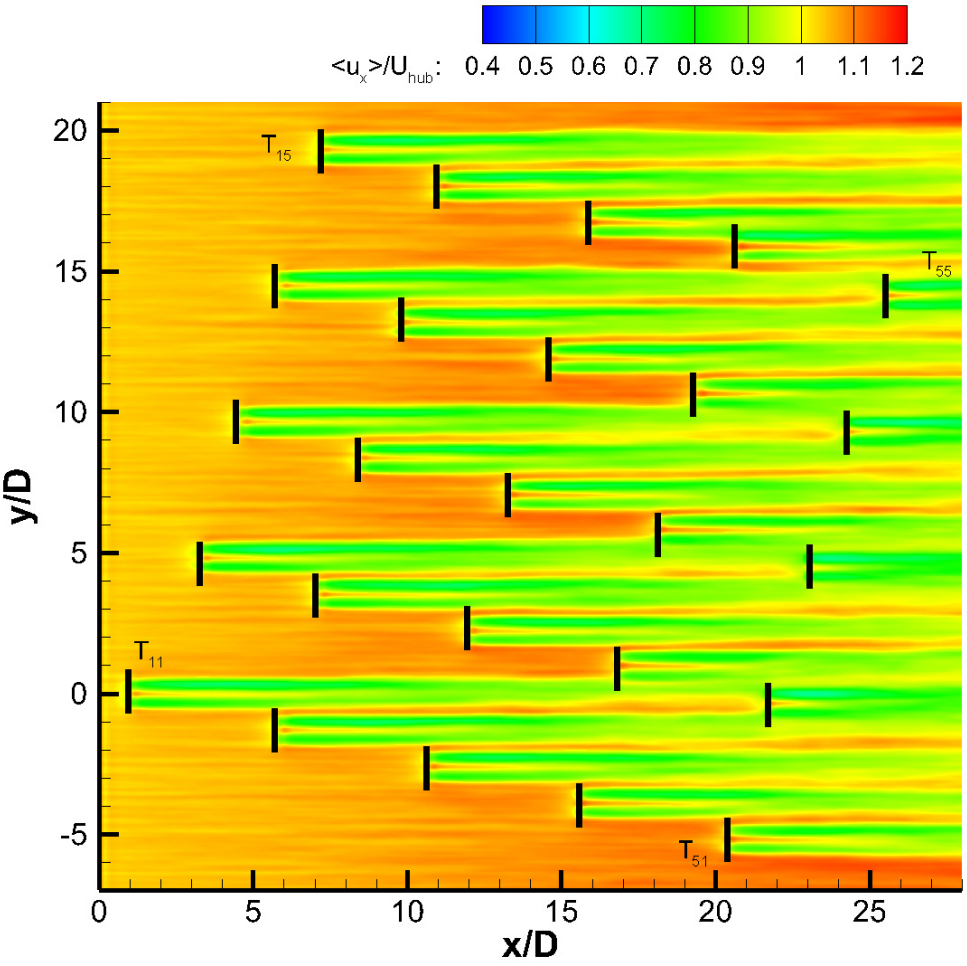

Figure 4.28. Normalized streamwise mean velocity at plane $z = 0$ under 5^o inflow angle.

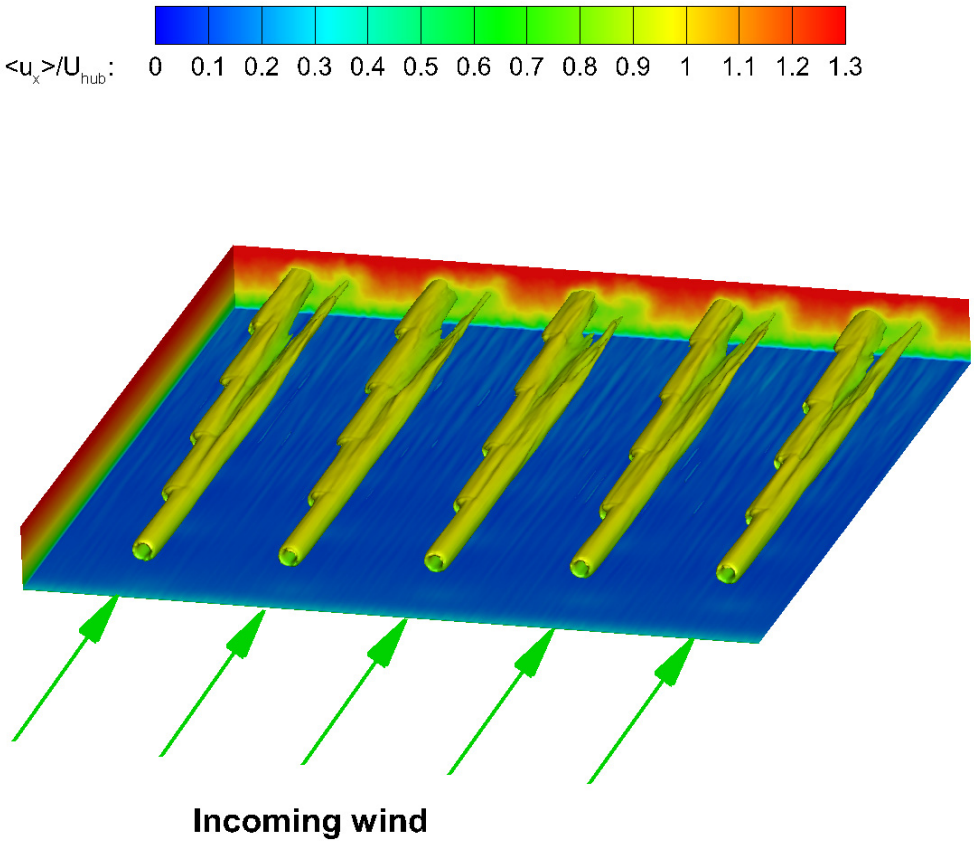

Figure 4.29. Isosurface of $U_{inlet} - < u_x >= 1$ m/s under 5^o inflow angle.

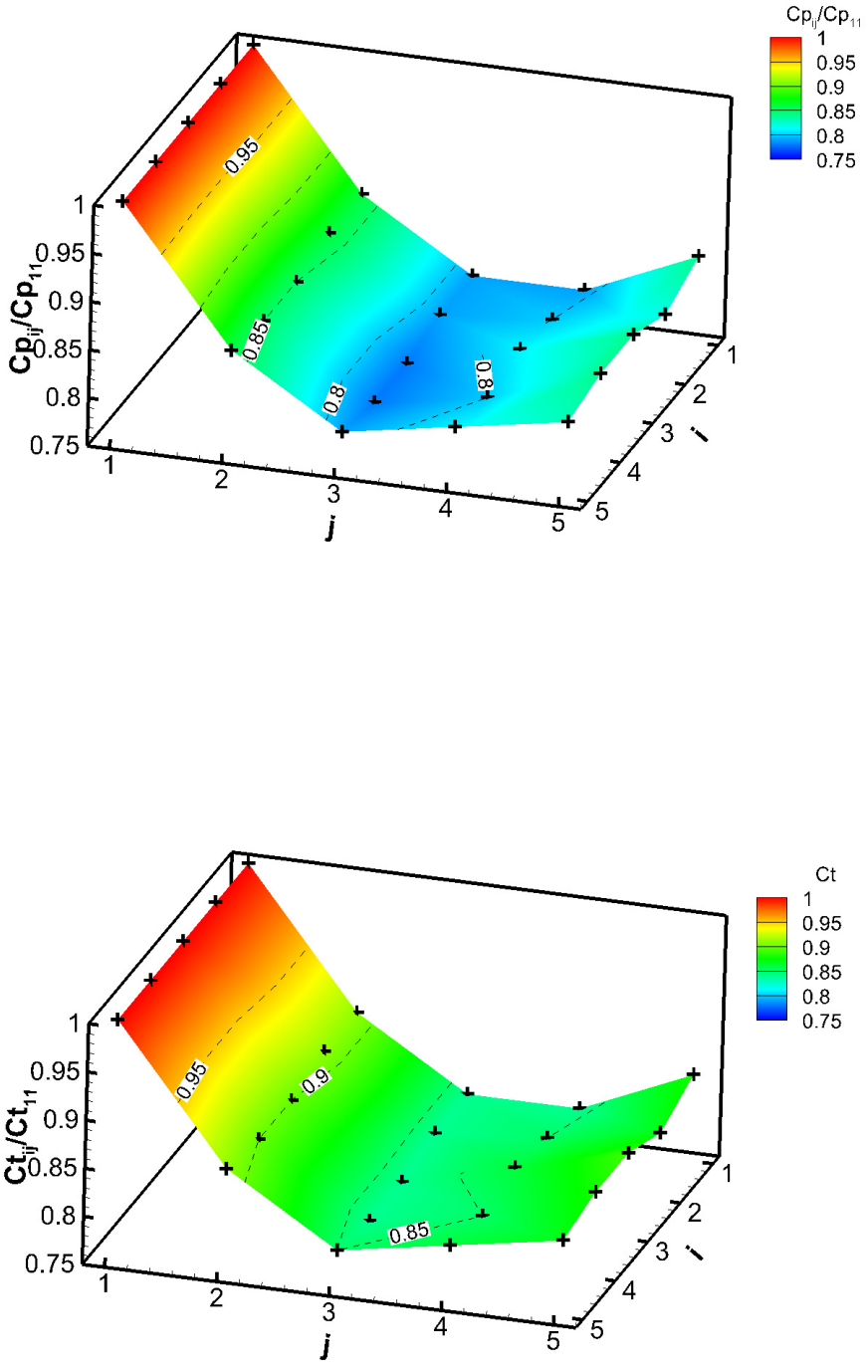

Figure 4.30. Distribution of normalized Cp and Ct under 5^o inflow angle.

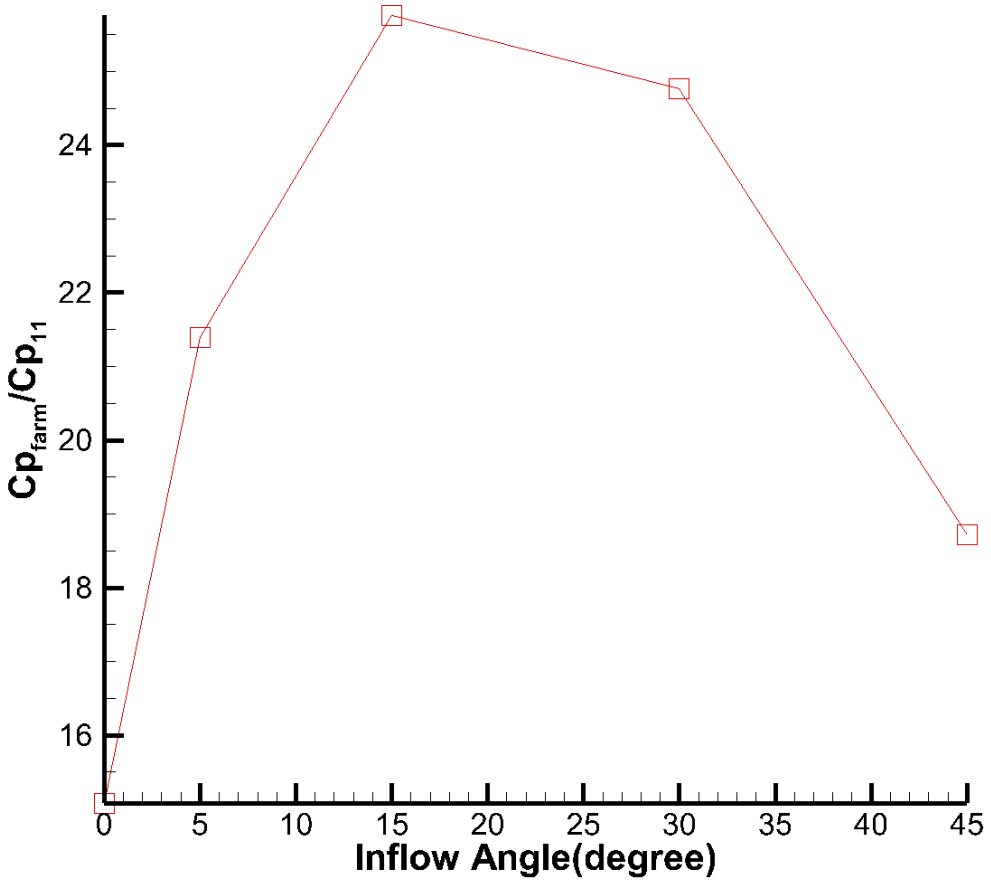

Figure 4.31. Normalized power output of the active wind farm under different inflow angles.

5. SUMMARY

In this paper, a LES-ALM solver is implemented in OpenFOAM. This solver is then performed on a stand alone NREL Phase VI turbine (10m diameter) to assess different methods used to determine the relative velocity between blade and wind. The results of Blade Element Momentum Theory (iterative process), local velocity sampling and Lagrange Euler interpolation are compared with experiment conducted by NREL and LES with exact turbine geometry. The power coefficient and thrust coefficient of LEI are the closest to the experiment results, compared with LVS and iterative process. The difference among these three methods are also analyzed. The advantage of LEI is that it can better capture the ratio of tangential component and the normal component of the relative velocity, which represents the angle of attack. Then LES-ALM with LEI is performed on a small wind farm with five NREL Phase VI turbines in full wake setting. The power outputs and thrust coefficients of downstream turbines are evaluated under turbulent inlet boundary condition generated by vortex method. Turbulence induced wake recovery are manifest. Although wake recovery can prevent the power outputs of downstream turbines from being too low, it still brings more severe aerodynamic loading fluctuation, which will affect the operation of downstream wind turbines. LES-ALM with LEI is also performed on a small wind farm deploying 25 (5×5) NREL Phase VI turbines. The power outputs and force coefficients of each

turbine are evaluated under different inflow angles (0^o, 5^o, 15^o, 30^o and 45^o). Velocity fields are also analyzed. The wake becomes more turbulent as the position goes downstream. The interactions between turbines do not only exist in the streamwise direction, but also in lateral directions. Partial wake setting can help increase power output of the wind farm For the proposed wind farm, a inflow angle near 15^o will produce the maximum power output. The results also demonstrate that the LES-ALM with LEI has the potential to optimize wind farm arrangement and pitch angle of individual turbines.

Future work includes the following aspects: (a) testing different turbulence model to find out which one is the most suitable one for LES-ALM with LEI; (b) adopting Immersed Boundary Method to model the effects of tower, nacelle and complex ground geometry; (c) calculating sound field based on the velocity and pressure fields generated by the LES solver; (d) implementing precursur simulation into OpenFOAM to get a better turbulent inflow condition.

LIST OF REFERENCES

LIST OF REFERENCES

[1] B. Sanderse, v. d. S. Pijl, and B. Koren, "Review of computational fluid dynamics for wind turbine wake aerodynamics," *Wind Energy*, vol. 14, no. 7, pp. 799–819, 2011.

[2] H. Neustadter and D. Spera, "Method for evaluating wind turbine wake effects on wind farm performance," *Journal of Solar Energy Engineering*, vol. 107, no. 3, pp. 240–243, 1985.

[3] B. Sanderse, "Aerodynamics of wind turbine wakes," *Energy Research Center of the Netherlands (ECN), ECN-E–09-016, Petten, The Netherlands, Tech. Rep*, 2009.

[4] M. M. Hand, D. Simms, L. Fingersh, D. Jager, J. Cotrell, S. Schreck, and S. Larwood, *Unsteady aerodynamics experiment phase V: test configuration and available data campaigns*. National Renewable Energy Laboratory, 2001.

[5] D. Simms, S. Schreck, M. Hand, and L. Fingersh, *NREL unsteady aerodynamics experiment in the NASA-Ames wind tunnel: A comparison of predictions to measurements*. National Renewable Energy Laboratory Colorado, USA, 2001.

[6] R. B. Cal, J. Lebrón, L. Castillo, H. S. Kang, and C. Meneveau, "Experimental study of the horizontally averaged flow structure in a model wind-turbine array boundary layer," *Journal of Renewable and Sustainable Energy*, vol. 2, no. 1, p. 013106, 2010.

[7] M. Adaramola and P.-Å. Krogstad, "Experimental investigation of wake effects on wind turbine performance," *Renewable Energy*, vol. 36, no. 8, pp. 2078–2086, 2011.

[8] R. Barthelmie, G. Larsen, S. Frandsen, L. Folkerts, K. Rados, S. Pryor, B. Lange, and G. Schepers, "Comparison of wake model simulations with offshore wind turbine wake profiles measured by sodar," *Journal of atmospheric and oceanic technology*, vol. 23, no. 7, pp. 888–901, 2006.

[9] F. Bingöl, J. Mann, and G. C. Larsen, "Light detection and ranging measurements of wake dynamics part i: one-dimensional scanning," *Wind Energy*, vol. 13, no. 1, pp. 51–61, 2010.

[10] G. V. Iungo, Y.-T. Wu, and F. Porté-Agel, "Field measurements of wind turbine wakes with lidars," *Journal of Atmospheric and Oceanic Technology*, vol. 30, no. 2, pp. 274–287, 2013.

[11] J. Hong, M. Toloui, L. P. Chamorro, M. Guala, K. Howard, S. Riley, J. Tucker, and F. Sotiropoulos, "Natural snowfall reveals large-scale flow structures in the wake of a 2.5-mw wind turbine," *Nature communications*, vol. 5, 2014.

[12] Y. Wu and F. Porté-Agel, "Large-eddy simulation of wind-turbine wakes: evaluation of turbine parametrisations," *Boundary-layer meteorology*, vol. 138, no. 3, pp. 345–366, 2011.

[13] X. Yang, F. Sotiropoulos, R. J. Conzemius, J. N. Wachtler, and M. B. Strong, "Large-eddy simulation of turbulent flow past wind turbines/farms: the virtual wind simulator (vwis)," *Wind Energy*, 2014.

[14] P. K. Jha, M. J. Churchfield, P. J. Moriarty, and S. Schmitz, "Guidelines for volume force distributions within actuator line modeling of wind turbines on large-eddy simulation-type grids," *Journal of Solar Energy Engineering*, vol. 136, no. 3, p. 031003, 2014.

[15] R. J. Stevens, J. Graham, and C. Meneveau, "A concurrent precursor inflow method for large eddy simulations and applications to finite length wind farms," *Renewable Energy*, vol. 68, pp. 46–50, 2014.

[16] J. Sørensen and W. Shen, "Numerical modeling of wind turbine wakes," *Journal of fluids engineering*, vol. 124, no. 2, pp. 393–399, 2002.

[17] J.-O. Mo and Y.-H. Lee, "Cfd investigation on the aerodynamic characteristics of a small-sized wind turbine of nrel phase vi operating with a stall-regulated method," *Journal of mechanical science and technology*, vol. 26, no. 1, pp. 81–92, 2012.

[18] H. Lu and F. Porté-Agel, "Large-eddy simulation of a very large wind farm in a stable atmospheric boundary layer," *Physics of Fluids (1994-present)*, vol. 23, no. 6, p. 065101, 2011.

[19] F. Porté-Agel, H. Lu, and Y.-T. Wu, "Interaction between large wind farms and the atmospheric boundary layer," *Procedia IUTAM*, vol. 10, pp. 307–318, 2014.

[20] N. Zhou, J. Chen, D. Adams, and S. Fleeter, "Influence of inflow conditions on turbine loading and wake structures predicted by direct large eddy simulations."

[21] F. Zahle, N. N. Sørensen, and J. Johansen, "Wind turbine rotor-tower interaction using an incompressible overset grid method," *Wind Energy*, vol. 12, no. 6, pp. 594–619, 2009.

[22] H. Glauert, "Airplane propellers, aerodynamic theory, edited by wf durand," 1963.

[23] J. Sørensen, W. Shen, and X. Munduate, "Analysis of wake states by a full-field actuator disc model," *Wind Energy*, vol. 1, no. 2, pp. 73–88, 1998.

[24] R. Mikkelsen, J. Sørensen, and W. Shen, "Modelling and analysis of the flow field around a coned rotor," *Wind Energy*, vol. 4, no. 3, pp. 121–135, 2001.

[25] R. Mikkelsen, "Actuator disc methods applied to wind turbines," Ph.D. dissertation, Technical University of Denmark, 2003.

[26] S. Ivanell, J. Sørensen, and D. Henningson, *Numerical computations of wind turbine wakes*. Springer, 2007.

[27] N. Troldborg, J. Sørensen, and R. Mikkelsen, "Actuator line modeling of wind turbine wakes," Ph.D. dissertation, Technical University of DenmarkDanmarks Tekniske Universitet, Department of Energy EngineeringInstitut for Energiteknik, 2008.

[28] P.-E. Réthoré, "Wind turbine wake in atmospheric turbulence," 2009.

[29] F. Porté-Agel, Y. Wu, H. Lu, and R. Conzemius, "Large-eddy simulation of atmospheric boundary layer flow through wind turbines and wind farms," *Journal of Wind Engineering and Industrial Aerodynamics*, vol. 99, no. 4, pp. 154–168, 2011.

[30] W. Z. Shen, J. H. Zhang, and J. N. Sørensen, "The actuator surface model: a new navier–stokes based model for rotor computations," *Journal of Solar Energy Engineering*, vol. 131, no. 1, p. 011002, 2009.

[31] C. Sibuet Watters, S. Breton, and C. Masson, "Application of the actuator surface concept to wind turbine rotor aerodynamics," *Wind Energy*, vol. 13, no. 5, pp. 433–447, 2010.

[32] L. A. Martınez, S. Leonardi, M. J. Churchfield, and P. J. Moriarty, "A comparison of actuator disk and actuator line wind turbine models and best practices for their use," *AIAA Paper*, no. 2012-0900, 2012.

[33] M. Shives and C. Crawford, "Mesh and load distribution requirements for actuator line cfd simulations," *Wind Energy*, vol. 16, no. 8, pp. 1183–1196, 2013.

[34] T. Burton, N. Jenkins, D. Sharpe, and E. Bossanyi, *Wind energy handbook*. John Wiley & Sons, 2011.

[35] S. Lee, S. K. Lele, and P. Moin, "Simulation of spatially evolving turbulence and the applicability of taylors hypothesis in compressible flow," *Physics of Fluids A: Fluid Dynamics (1989-1993)*, vol. 4, no. 7, pp. 1521–1530, 1992.

[36] K. Kondo, S. Murakami, and A. Mochida, "Generation of velocity fluctuations for inflow boundary condition of les," *Journal of Wind Engineering and Industrial Aerodynamics*, vol. 67, pp. 51–64, 1997.

[37] C. D. Pierce and P. Moin, "Method for generating equilibrium swirling inflow conditions," *AIAA journal*, vol. 36, no. 7, pp. 1325–1327, 1998.

[38] P. Wang, X.-S. Bai, M. Wessman, and J. Klingmann, "Large eddy simulation and experimental studies of a confined turbulent swirling flow," *Physics of Fluids (1994-present)*, vol. 16, no. 9, pp. 3306–3324, 2004.

[39] P. Druault, S. Lardeau, J.-P. Bonnet, F. Coiffet, J. Delville, E. Lamballais, J.-F. Largeau, and L. Perret, "Generation of three-dimensional turbulent inlet conditions for large-eddy simulation," *AIAA journal*, vol. 42, no. 3, pp. 447–456, 2004.

[40] E. Sergent, "Vers une methodologie de couplage entre la simulation des grandes echelles et les modeles statistiques," Ph.D. dissertation, Ecully, Ecole centrale de Lyon, 2002.

[41] F. Mathey, D. Cokljat, J. P. Bertoglio, and E. Sergent, "Assessment of the vortex method for large eddy simulation inlet conditions," *Progress in Computational Fluid Dynamics, An International Journal*, vol. 6, no. 1, pp. 58–67, 2006.

[42] J. Smagorinsky, "General circulation experiments with the primitive equations: I. the basic experiment*," *Monthly weather review*, vol. 91, no. 3, pp. 99–164, 1963.

[43] W. Z. Shen, R. Mikkelsen, J. N. Sørensen, and C. Bak, "Tip loss corrections for wind turbine computations," *Wind Energy*, vol. 8, no. 4, pp. 457–475, 2005.

[44] W. Z. Shen, J. N. Sørensen, and R. Mikkelsen, "Tip loss correction for actuator/navier–stokes computations," *Journal of Solar Energy Engineering*, vol. 127, no. 2, pp. 209–213, 2005.

[45] X. Yang, X. Zhang, Z. Li, and G.-W. He, "A smoothing technique for discrete delta functions with application to immersed boundary method in moving boundary simulations," *Journal of Computational Physics*, vol. 228, no. 20, pp. 7821–7836, 2009.

[46] N. Jarrin and R. Prosser, *Synthetic inflow boundary conditions for the numerical simulation of turbulence*. University of Manchester, 2008.

[47] G. Tabor and M. Baba-Ahmadi, "Inlet conditions for large eddy simulation: a review," *Computers & Fluids*, vol. 39, no. 4, pp. 553–567, 2010.

[48] *OpenFOAM user guide*. OpenFOAM Foundation, 2011.

[49] C. Rhie and W. Chow, "Numerical study of the turbulent flow past an airfoil with trailing edge separation," *AIAA journal*, vol. 21, no. 11, pp. 1525–1532, 1983.

[50] R. Issa, "Solution of the implicitly discretized fluid flow equations by operator-splitting, journal of computational physics," *Journal of Computational Physics*, vol. 62, pp. 40–65, 1985.

[51] B. Blocken, T. Defraeye, D. Derome, and J. Carmeliet, "High-resolution cfd simulations for forced convective heat transfer coefficients at the facade of a low-rise building," *Building and Environment*, vol. 44, no. 12, pp. 2396–2412, 2009.

[52] T. Defraeye, B. Blocken, and J. Carmeliet, "Cfd analysis of convective heat transfer at the surfaces of a cube immersed in a turbulent boundary layer," *International Journal of Heat and Mass Transfer*, vol. 53, no. 1, pp. 297–308, 2010.

[53] J. Liu, J. Srebric, and N. Yu, "Numerical simulation of convective heat transfer coefficients at the external surfaces of building arrays immersed in a turbulent boundary layer," *International Journal of Heat and Mass Transfer*, vol. 61, pp. 209–225, 2013.

[54] Z. Yang, P. Sarkar, and H. Hu, "Visualization of the tip vortices in a wind turbine wake," *Journal of visualization*, vol. 15, no. 1, pp. 39–44, 2012.

[55] R. J. Barthelmie, O. Rathmann, S. T. Frandsen, K. Hansen, E. Politis, J. Prospathopoulos, K. Rados, D. Cabezón, W. Schlez, J. Phillips *et al.*, "Modelling and measurements of wakes in large wind farms," in *Journal of Physics: Conference Series*, vol. 75, no. 1. IOP Publishing, 2007, p. 012049.